

Elastic turbulence in curvilinear flows of polymer solutions.

Alexander Groisman^a and Victor Steinberg^b

^aDepartment of Physics, UCSD, 9500 Gilman Dr., La Jolla, CA 92093-0374, USA,

^bDepartment of Physics of Complex Systems, Weizmann Institute of Science, Rehovot 76100, Israel
(September 18, 2018)

Following our first report (A. Groisman and V. Steinberg, *Nature* **405**, 53 (2000)) we present an extended account of experimental observations of elasticity induced turbulence in three different systems: a swirling flow between two plates, a Couette-Taylor (CT) flow between two cylinders, and a flow in a curvilinear channel (Dean flow). All three set-ups had high ratio of width of the region available for flow to radius of curvature of the streamlines. The experiments were carried out with dilute solutions of high molecular weight polyacrylamide in concentrated sugar syrups. High polymer relaxation time and solution viscosity ensured prevalence of non-linear elastic effects over inertial non-linearity, and development of purely elastic instabilities at low Reynolds number (Re) in all three flows. Above the elastic instability threshold, flows in all three systems exhibit features of developed turbulence. Those include: (i) randomly fluctuating fluid motion excited in a broad range of spatial and temporal scales; (ii) significant increase in the rates of momentum and mass transfer (compared to those expected for a steady flow with a smooth velocity profile). Phenomenology, driving mechanisms, and parameter dependence of the elastic turbulence are compared with those of the conventional high Re hydrodynamic turbulence in Newtonian fluids. Some similarities as well as multiple principal differences are found. In two out of three systems (swirling flow between two plates and flow in the curvilinear channel) power spectra of velocity fluctuations are decaying rather quickly, following power laws with exponents of about -3.5. It suggests that being random in time, the flow is rather smooth in space, in the sense that the main contribution to deformation and mixing (and, possibly, elastic energy) is coming from flow at the largest scale of the system. This situation - random in time and smooth in space - is analogous to flows at small scales (below Kolmogorov dissipation scale) in high Re turbulence.

47.27.-i,47.50.+d,83.50.-v

I. INTRODUCTION.

Turbulence is one of the most fascinating phenomena in nature and one of the biggest challenges for modern physics. It is common knowledge that a flow of a simple, low molecular, Newtonian fluid is likely to be turbulent, when velocity, V , is high, kinematic viscosity of the fluid, ν , is low, and size of the tank, L , is large. All these three factors contribute to high value of the Reynolds number, $Re = VL/\nu$. Motion of the Newtonian fluids is governed by the Navier-Stokes equation [1]

$$\frac{\partial \vec{V}}{\partial t} + (\vec{V} \vec{\nabla}) \vec{V} = -\nabla p/\rho + \nu \Delta \vec{V}, \quad (1)$$

where p is pressure and ρ is density of the fluid. The equation has a non-linear term, $(\vec{V} \vec{\nabla}) \vec{V}$, which is inertial in its nature. The Reynolds number defines the ratio of this non-linear term to the viscous dissipative term, $\nu \Delta \vec{V}$. When Re is high, the non-linear effects are strong, and the flow is likely to be turbulent. Therefore, turbulence in fluids at high Re is a paradigm for a strongly non-linear phenomenon in spatially extended systems [1,2].

Solutions of flexible high molecular weight polymers are visco-elastic liquids, and they differ from Newtonian fluids in many aspects [3]. The most striking elastic property of the polymer solutions is, probably, dependence of

mechanical stresses in flow on history of the flow. So, the stresses do not immediately become zero when fluid motion stops, but rather decay with some characteristic relaxation time, λ , which can be well above a second. When a polymer solution is sufficiently dilute, its stress tensor, τ , can be divided into two parts, $\tau = \tau_s + \tau_p$. The first part, τ_s , is defined by viscosity of the Newtonian solvent, η_s , and rate of strain in the flow, $\tau_s = -\eta_s [\vec{\nabla} \vec{V} + (\vec{\nabla} \vec{V})^T]$. So, the equation of motion for a dilute polymer solution becomes

$$\frac{\partial \vec{V}}{\partial t} + (\vec{V} \vec{\nabla}) \vec{V} = -\vec{\nabla} p/\rho + (\eta_s/\rho) \Delta \vec{V} - \nabla \tau_p/\rho \quad (2)$$

Here the elastic stress tensor, τ_p , is due to the polymer molecules, which are stretched in the flow, and it depends on history of the flow. One can see that τ_p enters the equation of motion linearly. So the degree of non-linearity of the equation of motion can still be defined by the Reynolds number, $Re = VL\rho/\eta_s$.

The simplest model incorporating the elastic nature of the polymer stress tensor, τ_p , is a Maxwell type constitutive equation [3] with a single relaxation time, λ ,

$$\tau_p + \lambda \frac{D\tau_p}{Dt} = -\eta_p [\vec{\nabla} \vec{V} + (\vec{\nabla} \vec{V})^T]. \quad (3)$$

Here $\frac{D\tau_p}{Dt}$ is a material time derivative of the polymer stress. An appropriate expression for the time derivative

$\frac{D\tau_p}{Dt}$ has to take into account that the stress is carried by fluid elements, which move, rotate and deform in the flow. The translational motion implies an advection term $(\vec{V}\vec{\nabla}) \cdot \tau_p$ in an appropriate expression for $\frac{D\tau_p}{Dt}$, while the rotation and deformation of the fluid particles should lead to contributions like $(\vec{\nabla}\vec{V}) \cdot \tau_p$ or $\tau_p \cdot (\vec{\nabla}\vec{V})$ [3]. Therefore, along with terms linear in τ_p and \vec{V} , some non-linear terms, in which τ_p is coupled to \vec{V} , should appear in the constitutive relation. A simple model equation for $\frac{D\tau_p}{Dt}$, which is commonly used for description of dilute polymer solutions, is the upper convected time derivative,

$$\frac{D\tau_p}{Dt} = \frac{\partial \tau_p}{\partial t} + (\vec{V}\vec{\nabla}) \cdot \tau_p - (\vec{\nabla}\vec{V})^T \cdot \tau_p - \tau_p \cdot (\vec{\nabla}\vec{V}). \quad (4)$$

The equations (3,4) together with the expression for τ_s constitute the Oldroyd-B model of polymer solution rheology [3]. One can see that non-linear terms in the constitutive equation (Eqs. 3,4) are all of the order $\lambda(V/L)\tau_p$. The ratio of those non-linear terms to the linear relaxation term, τ_p , is given by a dimensionless expression $\lambda(V/L)$, which is usually called Weissenberg number, Wi . (The relaxation term τ_p is somewhat analogous to the dissipation term in the Navier-Stokes equation.)

One can expect mechanical properties of the polymer solutions to become notably non-linear at sufficiently large Weissenberg numbers. Indeed, quite a few effects originating from the non-linear polymer stresses have been known for a long time [3]. So, in a simple shear flow of a polymer solution there is a difference between normal stresses along the direction of the flow and along the direction of velocity gradient. At low shear rates this normal stress difference, N_1 , is proportional to the shear rate squared. When flow lines are curvilinear, it gives rise to a volume force acting on the liquid in the direction of the curvature, the "hoop stress". Therefore, if a rotating rod is inserted in an open vessel with a highly elastic polymer solution, the liquid starts to climb up on the rod, instead of being pushed outwards [4]. This phenomenon is known as "rod climbing", or "Weissenberg effect". Further, in an purely extensional flow resistance of a polymer solution depends on rate of extension in a strongly non-linear fashion. There is a sharp growth in the elastic stresses, when the rate of extension exceeds $1/(2\lambda)$, that is at $Wi > 1/2$. As a result apparent viscosity of a dilute polymer solution can increase by up to three orders of magnitude [5]. Both the Weissenberg effect and the growth of the extensional flow resistance have been most clearly observed in very viscous polymer solutions and in flows with quite low Re , when non-linear inertial effects were insignificant.

A natural question arising here is, whether there may exist some kind of turbulent flow produced by the non-linear polymer stresses alone, in the absence of any significant inertial effects, at low Re . An important step in this direction was made about a decade and a half

ago when purely elastic instabilities were experimentally identified in a rotational flow between two plates [6] and in the Couette-Taylor (CT) flow between two cylinders [7]. The experiments were carried out with a Boger fluid [8], a dilute solution of high molecular weight polymers in a viscous Newtonian solvent. The Boger fluids are almost universally used as model viscoelastic fluids. Their relaxation times can be quite large, reaching seconds or even minutes, while their rheological properties are semi-quantitatively described by the simple Oldroyd-B model. The purely elastic instabilities occurred at Wi of order unity and vanishingly small Re . As a result of the instabilities, secondary vortex flows developed [7], and flow resistance somewhat increased [6]. The problem of linear stability of the CT flow was also treated theoretically using the Oldroyd-B model [9]. The analysis showed that the non-linear mechanical properties of the polymer solution can indeed lead to a flow instability, and a simple mechanism of this purely elastic instability was proposed.

During the past decade the purely elastic instabilities in the Boger fluids have been a subject of many theoretical and experimental studies, which are partially reviewed in Ref. [10,11]. After the pioneering work by Larson, Muller and Shaqfeh [7,9], purely elastic instabilities were also found in other shear flows with curvilinear streamlines. Those included the flow between a rotating cone and a plate and the Taylor-Dean flow [10,11]. The original theoretical analysis of Ref. [9] was refined, and more elaborate experiments were carried out. A few new mechanisms of flow instability driven by non-linear elastic stresses were suggested for cone-and-plate and for Taylor-Dean flows. The original mechanism proposed in Ref. [7] was verified experimentally in Ref. [12].

Some flow patterns observed above the purely elastic instability threshold in the curvilinear flows had rather disordered appearance and exhibited chaotic spectra of velocities. So, it was reasonable to suggest that at some conditions a truly turbulent flow might be excited by elastic stresses at vanishingly small Re . This idea was explicitly stated in Ref. [13], where analogy between elastic and inertial flow transitions was discussed. In fact, irregular flow patterns and growth of flow resistance in elastic polymer solutions at low Re were observed even before the purely elastic instabilities were identified [14]. Those flow phenomena were even sometimes coined "elastic turbulence". In all those cases, however, the term "turbulence" was used in a rather loose fashion, without being given a proper definition. More important, no quantitative data on either flow velocity field or spatial and temporal velocity spectra in those irregular flows were ever presented.

Although the notion of turbulence is widely used in scientific and technical literature, there is no unique commonly accepted definition of it. Therefore, turbulent flow is usually identified by its main features. Turbulence implies fluid motion in a broad range of temporal and spa-

tial scales, so that many degrees of freedom are excited in the system. There are no characteristic scales of time and space in the flow, except for those restricting the excited temporal and spatial domains from above and below. Turbulent flow is also usually accompanied by a significant increase in momentum and mass transfer. That is, flow resistance and rate of mixing in a turbulent flow become much higher than they would be in an imaginary laminar flow with the same Re .

In our recent publication [15] we showed, how the first three of these features of turbulence appeared in a flow of a highly elastic polymer solution at low Reynolds numbers. The experiments were done in a swirling flow between two plates with a wide gap, and the phenomenon was called elastic turbulence. In the present manuscript we give a more complete account of our experiments on the elasticity driven turbulent flow. We show additional velocity spectra, and distributions of probabilities of flow velocities and their derivatives. We also show that the elastic turbulence leads to quite efficient mixing in the flow. Further, we present results of our experiments on Couette-Taylor (CT) flow and on an open flow in a curvilinear channel (Dean flow), where we also observed the elasticity driven turbulence.

The paper is organized as follows. In the next section we discuss some practical problems concerning the experiment and the polymer solution. In Sections III, IV and V the results on the swirling flow between two plates, the CT flow and the flow in the curvilinear channel, respectively, are presented. The results are briefly summarized and discussed in Section VI.

II. EXPERIMENTAL CONSIDERATIONS.

As it was suggested in Ref. [13], where the CT flow was discussed, there is some analogy between flow transitions driven by elasticity and inertia. So, the inertially driven Taylor instability occurs at constant Taylor number [1,2], $Ta = \frac{d}{R} Re^2$, while the elastic instability is controlled by a parameter $K = \frac{\eta_p}{\eta} \frac{d}{R} Wi^2$ [9,12]. Here R is radius of the inner cylinder, d is width of the gap between the cylinders in the CT set-up, η is the total solution viscosity, and η_p is polymer contribution to the viscosity, $\eta_p \equiv \eta - \eta_s$. The Weissenberg number is defined here as $Wi = \lambda \Omega R / d$, where Ω is angular velocity of the rotating inner cylinder. (It was termed as the Deborah number in some of the original texts [9,12,13].) The Weissenberg number, which reflects non-linearity of the constitutive equation (Eqs. 3,4), appears to be analogous to the Reynolds number, which expresses non-linearity of the equation of motion. The geometric parameter determining curvature, the gap ratio, d/R , enters the expressions for both Ta and K . (There is also a specific term η_p/η , though, which shows polymer contribution to the solution viscosity and

naturally appears only in the expression for the parameter K for the elastic instability). Scales of time and velocity for the purely elastic flow transition are given by λ and d/λ , respectively. As it was shown in Ref. [13] they are analogous to t_{vd} and d/t_{vd} , which define scales of time and velocity for the inertially driven flow transitions. Here t_{vd} is the viscous diffusion time defined as $t_{vd} = d^2/\nu$.

Nevertheless, along with all those analogies, there are still some important differences between flow transitions driven by inertia and elasticity. So, it is an experimental fact that *any* laminar flow of a Newtonian fluid becomes unstable at sufficiently high Re , and all high Reynolds number flows are turbulent. That includes rectilinear shear flows, such as Poiseille flow in a circular pipe and plane Couette flow, which are supposed to be linearly stable at any Re . In contrast to it, purely elastic flow instabilities in shear flows have only been observed so far in systems with curvilinear stream lines. All these instabilities are supposed to be driven by the hoop stress, which originates from the normal stress differences. Elastic instabilities also occur in flows of polymer solutions with open surfaces and in extensional flows through contractions in channels [10,16]. A particular feature of the latter flows is that the rate of strain changes along the flow lines, so that even the basic flow states are not stationary in the Langrangian sense. Instabilities in those flows are not discussed in this paper.

This difference between the inertial and elastic instabilities may originate, of course, from the distinct governing equations. There are, however, some purely practical factors that can explain rather well the lack of observations of purely elastic flow transitions in rectilinear shear flows. Inertial instabilities in rectilinear shear flows of Newtonian fluids occur at quite high Reynolds numbers. Those are typically about two orders of magnitude higher than Re at which curvilinear shear flows with large gap ratios, d/R , become unstable. A priory, one may suggest that rectilinear and curvilinear shear flows would have a similar relation between Wi at thresholds of the purely elastic flow instabilities as well. The problem is, however, that while it is rather easy to generate high Re flows with low viscosity Newtonian fluids, it is usually impossible to reach the corresponding high values of Wi in shear flows of elastic polymer solutions. That is, there always exist rather severe practical limitations restricting non-linearity in elastic polymer stresses in shear flows. Their molecular mechanisms have been recently elucidated in a seminal paper by Chu's group [17].

Polymer molecules have finite extensibility, and their relaxation time decreases when they get stretched in a shear flow. This thinning of the relaxation time at high Wi is usually quite a strong and well recognized effect. In fact, different variations of the basic Oldroyd-B model have been specially developed to take into account the shear thinning [3]. Significant decrease of λ with

shear rate, $\dot{\gamma}$, renders growth of the Weissenberg number, $Wi = \lambda(\dot{\gamma})\dot{\gamma}$, much slower than linear in $\dot{\gamma}$. Substantial stretching of the polymer molecules in the primary shear flow also reduces their ability for further extension and susceptibility of the elastic stresses to flow perturbations, which is necessary for generation of the flow instabilities and secondary vortex flows [9]. Finally, high shear rates cause mechanical degradation of the polymer molecules. It leads to permanent reduction of elasticity during experimental runs and decay of λ that can be very fast at high Wi . Because of all those reasons it was found to be very difficult or even impossible to observe elastic instabilities, when expected values of Wi at the instability threshold were high. It was the case in curvilinear flows with small gap ratios, d/R , [18] and small viscosity ratios η_p/η [12].

Therefore, in order to maximize the non-linear elastic effects and to get a better opportunity to observe the elastic turbulence we had to choose experimental conditions quite carefully [15]. First, it was important to obtain an elastic instability at a possibly low critical Weissenberg number, Wi_c . For that purpose the gap ratio and the viscosity ratio had to be possibly large. Therefore, we used a polymer solution with a rather large η_p/η of about 1/4. (Further increase of the polymer concentration and of η_p/η was not very efficient, and would also complicate the solution rheology, including large shear thinning of the solution viscosity.) In order to have a large gap ratio with a possibility to vary it, we carried out our experiments in a swirling flow between two plates. The ratios d/R which we used were 0.263 and 0.526. In fact, historically we first tested a CT flow with $d/R = 1/2$, but growth of flow resistance in it was significantly smaller than in the swirling flow set-up, which we studied later (see sections III-IV).

Second, an appropriate polymer sample for the solution had to be chosen, that would not suffer major mechanical degradation under experimental flow conditions. Further, the limit for extensibility of the polymer molecules had to be possibly high compared with their typical conformations at the instability threshold. We used Polyacrylamide (PAAm) with a large average weight $M_w = 18,000,000$ and a broad molecular weight distribution (and low concentration of polyacrylic acid monomers) supplied by Polysciences. This commercial polymer sample proved to be remarkably stable with respect to mechanical degradation, that allowed us to reach high values of Wi and to explore strongly non-linear flow regimes. The high molecular weight of the polymers resulted in a large characteristic relaxation time, λ , even with solvents of moderate viscosity, and in a small characteristic stress, $\tau_0 = \eta_s/\lambda$. One can learn from the Eqs. 3,4 that τ_0 sets a scale of the polymer stress, at which its non-linearity becomes significant. Therefore, the value of τ_0 together with η_p/η and d/R determine the polymer stress τ_p in the primary shear flow at the

instability threshold. It is rather natural to suggest that when polymer molecules transduce less stress, they are also less subjected to mechanical degradation. Further, molecular interpretation of the Weissenberg number in a shear flow is the degree of deformation of polymer molecules from their relaxed random coil conformations. So, $Wi = 1$ can be regarded as a characteristic value at which extension of polymer molecules becomes considerably larger than the size of relaxed coils. By the same token, extension of a polymer molecule at Wi_c (the elastic instability threshold) is supposed to be a fixed multiple of the relaxed coil size (in the first, linear approximation valid at moderate Wi_c [17]). High molecular weight and flexibility of a polymer suggests large number of the Kuhn segments [3,19] in the polymer chain, and a high ratio between its contour length (size, when fully extended) and the size (radius of gyration, R_g) of a relaxed coil. (For a polymer molecule in a good solvent, with $R_g \sim M_w^{3/5}$, this ratio should increase as $M_w^{2/5}$ [19]. We would like to point out here that addition of 1% of NaCl to the solution significantly reduced R_g .) Therefore, using a higher M_w polymer we increase "reserve" of extensibility starting from the typical conformation at Wi_c . That opens a way for reacher flow dynamics above the elastic instability threshold.

III. SWIRLING FLOW BETWEEN TWO PLATES.

A. Experimental set-up and procedure.

The experimental apparatus is schematically shown in Fig.1. Polymer solution was held in a stationary cylindrical cup with a flat bottom (lower plate). A coaxial rotating upper plate was just touching the surface of the fluid. The cup was mounted on top of a commercial rheometer, AR-1000 of TA-instruments. The upper plate was attached to the shaft of the rheometer, which allowed precise control of its rotation velocity, Ω , and measurements of the torque, T . The average shear stress at the upper plate, τ_w , was calculated using the equation $T = \tau_w \int r dS$, that gave $\tau_w \equiv 3T/(2\pi R^3)$. (The integration is over the upper plate surface.)

Sidewalls of the cup were machined of a single piece of perspex, which was optically clear. The cup was circular from the inside and square from the outside in horizontal cross-section. That allowed measurements of flow velocity in the horizontal plane by a laser Doppler velocimeter (LDV) with two crossing frequency shifted beams. By appropriate positioning and orientation of the beam crossing region, azimuthal (longitudinal) and radial (spanwise) velocity components, V_ϕ and V_r , respectively, could be measured at different r and z . Here

(r, ϕ, z) are cylindrical coordinates. The bottom of the cup was machined of stainless steel and the temperature was stabilized at 12 °C by circulation of water below the bottom plate.

A slightly modified version of the set-up was designed to photograph the flow from below and to observe mixing in the flow. A special cup of the same shape but with a transparent bottom (lower plate, made of perspex) was attached to the rheometer concentrically with the shaft but above the rheometer base, and a mirror tilted by 45° was placed under the cup, as it is schematically shown in Fig.1. The mirror was used both to illuminate the fluid by diffuse light and to relay images of the flow to a CCD camera. The camera was equipped with a regular video lens and mounted horizontally near the rheometer (Fig.1). The source of the diffuse light was an illuminated white screen around the camera. The images were digitized by an 8 bit 512x512 frame grabber. In order to provide thermal stabilization, in this case the whole rheometer was placed in a thermally isolated box with through flow of temperature controlled air.

In the basic standard set-up, the radii of the upper plate and of the cup were $R = 38$ mm and $R_2 = 43.6$ mm, respectively, and the distance between the plates was $d = 10$ mm. The configuration was similar to the devices with rotating flow between two plates used in experiments on purely elastic instability [6,11,18,20]. Its gap ratio, d/R , was significantly higher, though. In order to study dependence of flow conditions on size of the system, two smaller set-ups, a half-size and a quarter-size, with all the dimensions reduced by factors of two and four, respectively, were used. Every time, when dimensions of an experimental set-up are non-standard, it is stated explicitly in the text.

We prepared a stock solution of PAAm ($M_w = 18,000,000$ by Polysciences) and used it through the whole course of the experiments. First we dissolved 0.9 g of PAAm powder and 3 g of NaCl in 275 ml of deionized water by gentle shaking. (Addition of NaCl was necessary to improve solubility of PAAm.) Next the solution was mixed for 3 hours in a commercial mixer with a propeller at a moderate speed. The idea behind that procedure was to cause mechanical degradation PAAm molecules with the highest weights, and to "cut" a high M tail of the broad molecular weight distribution of the PAAm sample. In a solution with a broad distribution of polymer molecular weights the heaviest molecules, which are most vulnerable to mechanical degradation, may also make a major contribution to the solution elasticity. A possible negative effect of that is significant degradation of elasticity during experimental runs, and inconsistency of results of the experiments. We found empirically that the procedure of pre-degradation in the mixer leads to substantial reduction of the degradation during the experiments and to substantial improvement of their consistency [21]. Finally, 9 g of iso-Propanol was added to

the solution (to preserve it from aging) and water was added up to 300 g. The final concentrations of PAAm, NaCl and iso-Propanol in the stock solution were 3000 ppm, 1% and 3%, respectively.

As a viscous Newtonian solvent for PAAm, we used a solution of 65% sugar (saccharose) and 1% NaCl in water. The salt was added to fix the ionic contents. Viscosity and relaxation time were measured with the same AR-1000 rheometer in a temperature controlled narrow gap Mooney-Ewart geometry. The solvent viscosity was $\eta_s = 0.324$ Pa·s at 12 °C. The PAAm concentration was 80 ppm, Fig.2. Solution viscosity, $\eta(\dot{\gamma})$, was carefully measured in a broad range of shear rates, $\dot{\gamma}$, Fig.2. Viscosity, η , was slowly decreasing with $\dot{\gamma}$, so that its shear thinning was about 7% per a decade of $\dot{\gamma}$. At a shear rate of $\dot{\gamma} = 1$ s⁻¹, corresponding to the onset of a purely elastic instability in the standard configuration (see below), η was 0.424 Pa·s, and the viscosity ratio was $\eta_p/\eta = 0.235$. Polymer relaxation time, λ , was measured in oscillatory tests with a shear rate amplitude of 1 s⁻¹. Components of the apparent viscosity of the solution in phase and out of phase with the applied shear, η' and η'' , respectively, were measured in long series of oscillations in a range of angular frequencies, ω . (Individual series were typically repeated about 10 times, and average viscosity values were calculated.) The same procedure was applied then to the solvent, and its viscosity components, η'_s and η''_s , were calculated as well. (The latter was nearly zero and it was an important test of virtual absence of inertial effects and of general applicability of the procedure.) The values for the polymer in phase and out of phase viscosity were calculated then as, $\eta'_p = \eta' - \eta'_s$ and $\eta''_p = \eta'' - \eta''_s$. The (frequency dependent) relaxation time was calculated as $\lambda(\omega) = \tan^{-1}(\eta''_p/\eta'_p)/\omega$, and $\lambda(\omega)$ at $\omega \rightarrow 0$, estimated as 3.4 s, was chosen as a representative relaxation time, λ , inset in Fig.2. The diffusion coefficient for the saccharose molecules was about $D = 8.5 \cdot 10^{-7}$ cm²/s [22].

In a swirling flow between two plates shear rate is quite inhomogeneous over the fluid bulk, even when the flow is laminar. So, in the simplest case of a narrow gap, $d/R \ll 1$, when the shear rate is constant along the z -direction, it grows along the radius, from zero at $r = 0$ to the maximal value of $\Omega R/d$ at $r = R$. Shear rate averaged over the surface of the upper plate (and over the fluid volume) is then $2\Omega R/(3d)$. In our case, when the gap is quite wide ($d/R = 0.263$ in the standard configuration) and the sidewalls are close to the upper plate, the situation is even more complicated. The shear rate becomes strongly non-homogeneous along z in a large region of space corresponding to r beyond $R - d$. So, measurements of the ratio T/Ω in a laminar flow of a viscous Newtonian liquid gave a value 1.68 times larger, than a value calculated suggesting homogeneous shear rate along z . (The latter suggestion is not realistic for the large gap ratio set-up, of course.) This discrepancy is obviously due to a high shear rate layer near the upper

plate at large r . One can see that choice of a representative shear rate becomes somewhat arbitrary under these circumstances. We decided to consider the simple expression $\Omega R/d$ as a characteristic shear rate, and to define the Weissenberg number as $Wi = \lambda \Omega R/d$. The Reynolds number was defined as $Re = \Omega R d \rho / \eta$.

In order to evaluate growth of flow resistance due to elastic instability and irregular secondary flow in the system, the average shear stress near the upper plate, τ_w^{lam} , in an imaginary laminar shear flow at the same Ω had to be estimated. The stress, τ_w^{lam} , would depend on an average shear rate, $\dot{\gamma}_{av}$, at the upper plate, and on viscosity of the polymer solution, η , at this shear rate. An appropriate expression for it is $\tau_w^{lam} = \eta(\dot{\gamma}_{av})\dot{\gamma}_{av}$. The average shear rate, $\dot{\gamma}_{av}$, was estimated from measurements of the ratio τ_w/η_0 in laminar flow of a Newtonian fluid with a large viscosity, η_0 , at low Re . The shear rate in the laminar flow, calculated as $\dot{\gamma}_{av} = \tau_w/\eta_0$, was proportional to Ω , being $\dot{\gamma}_{av} = 1.12\Omega R/d$ in the standard configuration, and it gave a properly weighted average over the surface of the upper plate.

A suitable parameter characterizing growth of the flow resistance is the ratio of the average stress at the upper plate, τ_w (defined as $\tau_w \equiv 3T/(2\pi R^3)$ again), to the stress τ_w^{lam} in the laminar flow at the same Ω . In Newtonian fluids this ratio generally increases with Re as the flow becomes increasingly irregular, and magnitude of τ_w/τ_w^{lam} can be considered as a measure of strength of turbulence and of the turbulent resistance. In our standard set-up, when a low viscosity Newtonian fluid is used, τ_w becomes 30% higher than τ_w^{lam} at $Re = 70$. Therefore, $Re = 70$ can be regarded as a characteristic value, at which inertial effects in the flow become considerable.

B. Observation of elastic turbulence.

1. Flow resistance.

The first indication of a strongly non-linear state in the swirling flow was significant growth of the flow resistance above the elastic instability threshold. Dependence of τ_w/τ_w^{lam} on the shear rate, $\dot{\gamma} = \Omega R/d$, is shown in Fig. 3. The shear rate was gradually increased in time, very slowly (by about $10\% \text{ h}^{-1}$) in the transition region, $\dot{\gamma} = 0.8 - 1.1 \text{ s}^{-1}$, and faster below and above it. One can see a sharp transition in flow of the polymer solution (curve 1, black line), that occurs at $\dot{\gamma}$ of about 1 s^{-1} (corresponding to $Wi = 3.5$), and that is manifested in a significant increase in τ_w compared to the laminar flow. The Reynolds number at the transition point is about 0.3, so that the inertial effects are quite negligible there. The transition has pronounced hysteresis (gray line, corresponding to slow reduction of $\dot{\gamma}$), which is rather typical for the purely elastic flow instability [12]. The ratio τ_w/τ_w^{lam} keeps growing with the shear rate and at the

highest $\dot{\gamma}$ that has been reached the flow resistance is about 12 times larger than it would be in a laminar flow. In the same range of shear rates flow of the pure solvent, curve 3, is completely laminar and the ratio τ_w/τ_w^{lam} is unity within resolution of the rheometer (about 1%).

Growth of the resistance in the polymer solution flow becomes even larger, when the size of the gap is increased to 20 mm (2nd curve in Fig.3), and the gap ratio becomes 0.526. Then the ratio τ_w/τ_w^{lam} reaches a value of 19. For Newtonian fluids in the same flow geometry such growth of the flow resistance is found at Re of about $2 \cdot 10^4$. For flow in a circular pipe this value of τ_w/τ_w^{lam} is reached at $Re \simeq 10^5$, which is usually considered as a region of rather developed turbulence [1,2].

Mechanical degradation of the polymers was quite small at shear rates below 1.5 s^{-1} and 1 s^{-1} , for $d = 10 \text{ mm}$ and 20 mm , respectively. The dependencies of τ_w/τ_w^{lam} on $\dot{\gamma}$ were therefore reproducible in consecutive runs within about 1%. At higher shear rates degradation effects became appreciable. Thus, to ensure consistency of the results, time of measurements at high shear rates had to be made possibly short. So, for $\dot{\gamma}$ above 1.5 s^{-1} , curve 1, the shear rate was raised by about 7% per minute, and the measurement time was not sufficient to average out fluctuations of τ_w produced by the flow. Irregular undulations in curves 1 and 2 in Fig.3 at high $\dot{\gamma}$ are due to those fluctuations and the short time of averaging.

In spite of the short time of the experiments, the solution relaxation time, λ , typically decreased by up to 10% after runs of the kind shown by the curves 1 and 2. Nevertheless, a major part of the degradation occurred at the highest shear rates, above 5 s^{-1} and above 3.5 s^{-1} for the curves 1 and 2, respectively. Therefore, the data at lower shear rates can be regarded as quite consistent.

Resistance is an integral characteristic of a flow, and its fluctuations give some information about flow events on the scale of the whole system. In order to get information about characteristic frequencies of the flow on this integral scale, we measured spectra of fluctuations of angular velocity of the upper plate at constant applied torque, T . (AR-1000 is a stress controlled rheometer, so it was more feasible to apply a constant torque and to monitor rotation velocity, than to do it the other way around.) Spectra of fluctuations of Ω at a few T corresponding to different average shear rates (all above the transition point, $\dot{\gamma} \simeq 1 \text{ s}^{-1}$) are presented in Fig.4. Root mean squares, RMS, of fluctuations of the angular velocity, Ω_{rms} , were about 4% of its average values, $\bar{\Omega}$, for all T . Because of the low rotation rates and low oscillation frequencies, inertial effects associated with acceleration of the shaft of the rheometer and of the liquid were always quite small. ($I\dot{\Omega}_{rms}$ was less than 1% of $(T/\bar{\Omega})\Omega_{rms}$, where I is the moment of inertia of the system, and $\dot{\Omega}_{rms}$ is RMS of the time derivative of Ω .) So, the spectra in

Fig. 4 should reflect time scales of fluctuations of viscous and elastic stresses in the flow.

As the average shear rate is raised, the power of fluctuations, P , increases and characteristic frequencies become higher, Fig.4. The general form of the spectra remains very much the same, however. There are no distinct peaks, except for instrumental peaks at f , which are multiples of the average frequencies of the upper plate rotation, $\bar{\Omega}/(2\pi)$. Further, each spectrum has a broad region, spanning about a decade in frequencies, where dependence of P on f is close to a power law, $P \sim f^{-\alpha}$, with $\alpha \simeq 4.3$. (Some increase in the power of fluctuations at higher f is due to instrumental noise, and it was also measured in laminar flow of the pure solvent, curve 6 in Fig.4.) The power law dependence implies that flow events on the integral scale of the system occur in this whole region of frequencies. As it was argued above, excitation of fluid motion in a broad continuous range of frequencies is one of the characteristic features of turbulence.

2. Temporal and spatial spectra.

Time spectra of fluctuations of flow velocity in a point at different constant shear rates (all above the elastic instability threshold) are shown in Fig.5. One component of the velocity in the horizontal plane was measured with LDV in the center of the set-up, where its average value was zero. The shear rates, $\dot{\gamma}$, for the curves 1-5 were the same as the average shear rates for the curves 1-5, respectively, in Fig.4. The spectra in Fig.5 have the same general features as those in Fig.4. Power of the fluctuations and their characteristic frequencies increase with $\dot{\gamma}$, but the spectra remain very similar in their appearance. In particular, the spectra do not have distinct peaks, and do have broad regions of frequencies, where the power of fluctuations decays according to a power law $P \sim f^{-\alpha}$. (Flattening of the curves at high f is due to instrumental noise; see also discussion of Fig.16 below.) Again, for each spectrum the power law decay region spans about an order of magnitude in f , that implies excitation of the fluid motion in the whole range of the corresponding temporal scales. One can see that characteristic frequencies of fluctuations in a point and at the integral scale (cf. Fig.4 and Fig.5) are rather close. The exponent, α , is about 3.5, which is rather close to the exponent of 4.3 in Fig.4, and much larger than the Kolmogorov exponent of 5/3, found for velocity spectra of high Re inertial turbulence [1,2].

A few representative snapshots of the flow viewed from below are shown in Fig.6. In order to visualize the flow, the fluid was seeded with light reflecting flakes (1% of Kalliroscope liquid). The upper plate was black. So, the bright regions are those, where the flakes are oriented parallel to the upper plate. The patterns of the polymer

solution flow above the transition, at $Wi = 6.5$, Fig.6a-b, and at $Wi = 13$, Fig.6c-e, look quite irregular and exhibit structures of different sizes. One can see, however, that the structures tend to have a spiral-like form, which is probably imposed by the average azimuthal flow and circular symmetry of the set-up. Further, there is a dark spot in the middle, which appears in most of the snapshots. It corresponds to the center of a big persistent toroidal vortex, which has dimensions of the whole set-up (see also below). Direction of the vortical motion was inwards near the upper plate, downwards near the center and outwards near the lower plate. Average flow velocity along the radial direction was measured by LDV in a few points, and the results agreed quite well with presence of the big persistent toroidal vortex. Flow of the pure solvent at the same shear rate was completely laminar that can be learned from the snapshot in Fig.6f. It looks quite uniform up to some variation along the radial direction due to varying shear rate and inhomogeneity along the circumference due to somewhat uneven (and directed) illumination.

The visual impression of spatial disorder in the flow at high Wi is confirmed by a more careful analysis. Figure 7 shows average Fourier spectra of the brightness profiles at $Wi = 13$ along the diameter and along the circumference at $r = 2d$. The spectra were averaged over long series of flow pattern snapshots taken in consecutive moments of time. The wavelength is measured in units of d , so that the wave number, k , of unity corresponds to a length of $2\pi d$. Amplitude of fluctuations of the brightness along the circumference does not have any peaks and it exhibits a power law decay, $A \sim k^{-1}$, over almost a decade in the wave number domain. This implies that there are no selected wave numbers in the azimuthal direction and the fluid motion is excited in a broad range of spatial scales. (The plateau at high k may be due to restricted spatial resolution of the method of visualization that was used.)

The spectrum taken along the diameter shows a general tendency of power law decay in even broader range of wave numbers. However, it apparently differs from the azimuthal spectrum by a series of broad peaks, which may be due to the persistent toroidal vortex discussed above. The average flow shear rate and the local gap ratio, d/r , vary along the radius, so that the radial direction is not neutral. Thus, the flow is not structureless and homogeneous along the radial direction. The visualization of the flow with the light reflecting flakes does not provide direct information about the fluid velocity field. Therefore, the specific value of the exponent in the power law fit in Fig.7 does not have any special meaning.

In order to obtain quantitative information about spatial structure of the fluctuating velocity field, we explored velocity spectra in various off-center points, with non-zero average azimuthal velocity, \bar{V}_ϕ . Spectra of fluctuations of the radial component of velocity, V_r , at $\dot{\gamma} = 4 \text{ s}^{-1}$ ($Wi = 13.5$) at four different radii are shown in Fig.8.

They all were measured at $z = d/2$, where z is the distance from the upper plate. Root mean squares of the fluctuations in all four points were rather close, varying between 0.88 and 0.99 mm/s. The spectra in Fig.8 bear the same general features of turbulence as the spectra in Figs.4, 5 and 7 discussed above. They do not exhibit distinct peaks, and have broad regions of f , where the power of fluctuations, P decreases according to $P \sim f^{-\alpha}$.

One can learn from Fig.8 that as the point of measurement is moved away from the center, characteristic frequencies of the fluctuations become higher. The most reasonable explanation of that is growth of the average azimuthal velocity, \bar{V}_ϕ , which was 3.81 mm/s and 6.99 mm/s, at $r = 2d$ and $r = 3d$, respectively. So, the fluctuations of the velocity in time in these two points are mainly due to fluctuations in space, which are advected by the large mean flow velocity, \bar{V}_ϕ . Applying the Taylor hypothesis, we can view the spectra in time as spectra in space, with relation between the frequency and the wave number given by $k = 2\pi f/\bar{V}_\phi$. Then the power law decay regions in curves 3 and 4 imply that the fluid motion is excited in the whole corresponding ranges of k . The ranges of the spatial scales, where the motion is excited, span about an order of magnitude for the both curves. The exponents α in the power laws $P \sim f^{-\alpha}$ (and, so, $P \sim k^{-\alpha}$) are again quite large, about 3.6 for $r = 2d$ and about 3.3 for $r = 3d$. These large values of α imply that the power of fluctuations decays very quickly as the size of eddies decreases. The main contribution to fluctuations of both velocity and velocity gradients (the power of the latter should scale as $k^{-(\alpha-2)}$) should therefore be due to the largest eddies.

3. Mixing in the flow.

Mixing in the flow was observed using a droplet of black ink added to working fluid before rotation of the upper plate was started, Fig. 9. Using a micropipette the droplet was carefully placed near the center (at $r = 0$) at about a half of the fluid depth. The ink was dissolved in a concentrated sugar syrup, to match density of the droplet with the density of the working fluid. We used the half-size set-up with $R = 19$ mm, $R_2 = 21.9$ mm, $d = 5$ mm. The volume of the working fluid was about 9 ml, and the amount of the ink was 50 μ l. The upper plate was colored white and the fluid was viewed from below. So, regions without the ink appeared bright, whereas dark regions corresponded to positions in the (r, ϕ) plane, where the total amount of the ink across the fluid layer was large.

Consecutive stages of mixing in the polymer solution are shown in Fig.9. Rotation of the upper plate was abruptly started at $t = 0$ at a rate of 1 turn per 4.26 seconds, which corresponded to a shear rate $\dot{\gamma} = 5.6$ s $^{-1}$. It took about one minute for the irregular flow to develop,

after the rotation of the upper plate was started. (Development of the irregular flow was judged by growth of the flow resistance, which was saturated after about one minute, cf. [23].) So, no significant changes in the ink distribution occurred during the first 15 seconds (Fig.9). After 30 sec the ink became spread over the surface of the lower plate by the big toroidal vortex discussed above. In the snapshots taken at later moments of time (60, 90 and 120 sec in Fig.9) one can see many fine scale structures. Those can be either due to excitation of the fluid motion at small spatial scales or significant stretching of fluid elements along their Lagrangian trajectories by randomly fluctuating large scale eddies. The contrast of the patterns gradually decreases with the time that indicates progressing mixing. The pattern in the last snapshot, taken 8 minutes after the flow has been started, looks completely homogeneous. From the appearance of the mixing patterns in Fig.9, characteristic time of mixing can be estimated as 120 seconds, corresponding to about 30 full turns of the upper plate. The time required for mixing by molecular diffusion without macroscopic flow can be estimated as dR/D . Substituting for D the diffusion coefficient for the saccharose molecules, $D = 8.5 \cdot 10^{-7}$ cm 2 /s, we obtain a diffusion time of about 10 6 seconds, that is four orders of magnitude larger than the mixing time in the flow. (Diffusion time for suspended solid particles of the black ink could be significantly larger.)

Mixing in the flow of the pure solvent at the same shear rate is shown for comparison in Fig.10. One can see that distribution of the ink remained inhomogeneous even after 9 hours, although the ink became somewhat spread with the time. The Reynolds number was about 0.5, and there were some non-vanishing inertial effects in the flow. In particular, centrifugal force gave rise to a slow fluid motion out of the $r - \phi$ plane. This motion had a form of a big toroidal vortex with outflow near the upper plate and inflow near the lower plate. (So, this vortex spun in the direction opposite to that of the toroidal vortex produced by the elastic stresses.) The vortical motion stirred the fluid but it did not really mix it. So, when the set-up was viewed from a side, one could see that the ink did not get to the toroidal core of the vortex.

Summarizing the experimental results, we conclude that the flow of the elastic polymer solution at sufficiently high Wi has indeed all the main features of developed turbulence that were stated above. The fluid motion is excited in broad ranges of frequencies and wave numbers, both spanning about an order of magnitude. The flow is accompanied by dramatic increase in the rate of transfer of momentum and mass. By the strength of the turbulent resistance and by the span of scales in space and time, where the fluid motion is excited, the observed flow can be compared to turbulence of a Newtonian fluid in a pipe at Re of about 10 5 . This apparently turbulent fluid motion in the swirling flow between two plates

arises at very low Re , where inertial effects are negligible, solely because of the non-linear mechanical properties of the elastic polymer solution. We therefore call the phenomenon *elastic turbulence*. Distinctions between the elastic turbulence and the usual inertial turbulence, which is observed in Newtonian fluids at high Rey , are discussed in Section III.D below.

C. Further properties of the flow.

1. Flow structure and velocity profiles.

In order to learn more about velocity field generated by the elastic turbulence, we measured average velocity and RMS of the velocity fluctuations at different points. Profiles in z -direction of the average azimuthal velocity, \bar{V} , and of RMS of its fluctuations, V_{rms} , at different flow conditions are shown in Fig.11. (It was the standard set-up.) The measurements are done at $r = 2d$, that is rather far from the edge of the upper plate ($R - r = 1.8d$). Profile of \bar{V} in a low Re flow of the pure solvent is an almost straight line, curve 3. The elasticity driven turbulent flow significantly changes the distribution of \bar{V} . It produces a high shear rate layer near the upper plate, curve 1, and a low shear rate region near the middle of the gap (at $z/d = 0.5$). Such a distribution of \bar{V} is reminiscent of average velocity profiles in usual high Re turbulence. The perturbation of the \bar{V} profile becomes stronger when $\dot{\gamma}$ is increased, curve 2. In particular, the slope of the \bar{V} -curve at small z/d becomes larger that obviously corresponds to growth of τ_w/τ_w^{lam} with $\dot{\gamma}$ (Fig.3).

Fluctuations of the azimuthal velocity, curve 4 in Fig.11, are small near the upper plate, reach a maximum at $z/d \simeq 0.25$, and start to decrease at larger z . Again, such distribution of V_{rms} along z is reminiscent of velocity fluctuations in turbulent flows of Newtonian fluids [1,2]. RMS of fluctuations reaches a value of about $0.5d/\lambda$, so that rate of deformations produced by the fluctuating velocity field is on the order of $1/\lambda$. That implies an essentially non-linear relation between the rate of deformations and the fluctuating elastic stress. (It is discussed in more detail in the next section.) The maximal RMS of the velocity fluctuations at $\dot{\gamma} = 4 \text{ s}^{-1}$ was about 1.55 mm/s , that was about 7.5% of the upper plate velocity (V_{max}) at $r = 2d$ and about 25% of the local value of \bar{V} .

As one can learn from curves 1 and 2 in Fig.11, there is significant asymmetry in distribution of the average shear rate, $\partial\bar{V}/\partial z$, along z . The main decrease of \bar{V} occurs near the upper plate. So, at $\dot{\gamma} = 4 \text{ s}^{-1}$, \bar{V}/V_{max} becomes 0.5 at $z/d = 0.12$ and at $z/d = 0.5$ the average velocity is only $0.18V_{max}$. (Velocity profile near the lower plate could not be measured because of instrumental restrictions.) The uneven distribution of the shear

rate along z -direction should create an essentially inhomogeneous profile of N_1 along z . Indeed, in a laminar shear flow we have $N_1 = 2\eta_p\lambda\dot{\gamma}^2 = 2\tau_p\lambda\dot{\gamma}$ (where τ_p is the polymer contribution to the shear stress). Therefore, the high shear rate near the upper plate should generate large N_1 and large hoop stress there. A result of this large unbalanced hoop stress would be motion of the fluid near the upper plate inwards in the radial direction, which is quite consistent with our observation of the permanent toroidal vortex discussed above (see Fig.6). In fact the shape of the $\bar{V}(z)$ profiles in Fig.11, which is strongly asymmetric with respect to the mid-plane ($z = d/2$), is also consistent with the picture of a *single* large scale toroidal vortex. Indeed, even a possible increase in the slope of the $\bar{V}(z)$ profile near the lower plate still would not match the high shear at small z , and the vortical motion in the rz -plane should be mainly driven by the high hoop stress near the upper plate. In contrast, a symmetric $\bar{V}(z)$ profile would imply equally high hoop stress near the upper and the lower plate (and low hoop stress in the middle) that would produce a pattern of two toroidal vortices on top of each other.

In fact the turbulent $\bar{V}(z)$ -profiles of the kind shown by curves 1 and 2 in Fig.11 were not always stable, especially at larger gap ratios. So, in a system with $d/R = 0.563$ at $\dot{\gamma} = 2.5 \text{ s}^{-1}$ the high shear rate layer randomly moved between a vicinity of the upper plate and a vicinity of the lower plate with a typical residence time of a few tens of minutes and a transition time of about a minute. These fluctuations in the location of the high shear rate layer were accompanied by inversions of the spinning direction of the big toroidal vortex. When the main drop of \bar{V} occurred near the lower plate, it was its vicinity where the radial flow was directed inwards. Therefore, the asymmetry of the $\bar{V}(z)$ profile with respect to the $z = d/2$ plane (Fig.11) is indeed directly related with the large scale vortical flow.

Big toroidal vortices driven by the hoop stress are actually quite well known to appear in swirling flows of elastic fluids [3,24], and inhomogeneity of the shear rate profile in the primary laminar flow has long been recognized as their common origin. In our system this vortex first arises as a stationary structure at low shear rates. As it can be learned from Fig.3 (curve 1 at $\dot{\gamma} < 0.75 \text{ s}^{-1}$ and curve 2 at $\dot{\gamma} < 0.4 \text{ s}^{-1}$) the toroidal vortex leads to some increase in flow resistance even before the transition to the elastic turbulence. As it is suggested by the first three snapshots in Fig.9, the big toroidal vortex is also the first vortical motion to arise upon sudden inception of a shear rate, which is above the elastic instability threshold level. (Further redistribution of the average azimuthal velocity due to development of the turbulent flow should enhance this large scale vortical motion.) So, we can conclude that transition to the elastic turbulence in the swirling flow between two plates is mediated by this vortex. The vortex is always present in the flow, and it probably suf-

fers permanent instability and is permanently fluctuating, that may be an important mechanism of production of fluid motion at smaller scales. The toroidal vortex is providing a smooth, large scale velocity field, which is randomly fluctuating in time, and in which the liquid and the stress tensor imbedded in it are chaotically advected. This type of advection can create variations of stress in a range of smaller scales, which may cause small scale fluid motion [25,26]. (This would be analogous to generation of small scale concentration variations in chaotic mixing by large fluctuating vortices.)

The large scale vortical flow is a probable reason for low Wi at the elastic instability threshold, and for the very strong increase of resistance above the transition to elastic turbulence in the flow between two plates. Indeed, growth of the flow resistance in the CT flow at comparable Wi (Fig.18 below) is significantly smaller. This situation is somewhat similar to inertial turbulence in Newtonian fluids in the same systems. In the swirling flow between two plates a big toroidal vortex, which is driven by centrifugal force, causes transition to turbulence at quite low Re and provides a route of efficient energy transfer to the turbulent flow. Many instructive pictures of the toroidal vortex, its evolution and instabilities in inertial, inertia-elastic, and elasticity dominated flow regimes in a swirling flow set-up with larger gap ratios can be found in Ref. [24].

2. Velocity statistics in a point.

Characteristic probability distribution functions (PDF) of azimuthal and radial components of the flow velocity in the regime of elastic turbulence are shown in Fig.12a,b. These distributions were obtained from LDV measurements taken at $r = 2d$, $z = 0.25d$ at a shear rate of 4 s^{-1} . PDF's of the azimuthal and radial velocity can be fitted quite well by the functions $A_1 \cdot \exp[-(V - \bar{V}_\phi)^2/(2a_1^2) + 0.032(V - \bar{V}_\phi)^3/a_1^3]$ and $A_2 \cdot \exp[-(V - \bar{V}_r)^2/(2a_2^2) - 0.017(V - \bar{V}_r)^3/a_2^3]$, respectively. Here $\bar{V}_\phi = 6.34 \text{ mm/s}$ and $\bar{V}_r = -1.84 \text{ mm/s}$ are the average velocities; $a_1 = 1.55 \text{ mm/s}$ and $a_2 = 0.97 \text{ mm/s}$ are the RMS of fluctuations for the azimuthal and radial components, respectively. One can see that the both distributions have only minor skewness and are very close to Gaussians. (That skewness is probably due to the non-zero average velocity.)

Probability distribution functions for gradients of velocity (rates of deformation) in the longitudinal and transversal directions, obtained from the same LDV time series, are shown in Fig.13a and Fig.13b, respectively. The rates of deformation are multiplied by the relaxation time, λ , to make them dimensionless. The velocity gradients were estimated using the Taylor hypothesis, with smoothing over a distance of about 1.45 mm. The difference, ΔV , between consecutive velocity readings with

even time intervals of $\Delta t = 0.22 \text{ s}$ was divided by Δt and by the average velocity $\bar{V} = (\bar{V}_\phi^2 + \bar{V}_r^2)^{1/2} = 6.6 \text{ mm/s}$. One can see that the distributions of $\frac{\partial V_\phi}{r\partial\phi}$ and $\frac{\partial V_r}{r\partial\phi}$ can not be fitted by Gaussians. In contrast to the velocity distributions in Fig.12, the both PDF's in Fig.13 have well pronounced exponential tails, which imply significant intermittency of the velocity gradients. The situation of nearly Gaussian statistics of velocities and essentially non-Gaussian, strongly intermittent distributions of velocity gradients is actually quite typical for high Re inertial turbulence [27]. Hence, the elastic turbulence resembles high Re inertial turbulent flows in this respect.

D. Comparison with inertial turbulence at high Reynolds number.

1. Role of the elastic stresses.

Along with the apparent similarity in phenomenology between the elastic and inertial turbulence, there are also quite a few very important distinctions. An obvious reason for that is difference in the physical mechanisms, which underlie the two kinds of turbulent motion. Turbulence in Newtonian fluids is observed at high Re , when the equation of motion (Eq. 1) is strongly nonlinear. The nonlinear term in Eq. 1 is connected with kinematics of *translational motion* in a continuous medium and is due to fluid inertia. The elastic turbulence occurs at low Re , when nonlinearity of the equation of motion (Eq. 2) is negligible. The origin of the elastic turbulence is nonlinear dependence of the elastic stresses on rate of deformation in flow. (This nonlinear dependence is very well seen in the model constitutive relation, Eqs. 3,4.) The latter nonlinearity is connected with kinematics of *deformation* in a continuous medium, and it is due to finite relaxation time of polymer molecules. Therefore, one can suggest that in the case of the elastic turbulence it would be more relevant to study the field of stresses and of rates of deformations rather than the velocity field.

The products of the randomly varying rates of deformation ($\frac{\partial V_\phi}{r\partial\phi}$ and $\frac{\partial V_r}{r\partial\phi}$ in Fig.13) and λ can actually be viewed as different estimates for Weissenberg number, Wi' , of the fluctuating velocity field. The distributions in Fig.13 show that Wi' is rather often above unity, and RMS of its fluctuations estimated from Fig.13a is about 0.83. Fluctuations of the rate of deformation are directly connected with fluctuations of the elastic stresses by the constitutive relation (see Eqs. 3 and 4). Since the fluctuating Weissenberg number is rather high, this connection should be essentially nonlinear. Therefore, one can suggest that the field of τ_p in the elastic turbulence is highly complex and strongly intermittent. It would certainly be quite instructive to explore spatial structure and temporal distribution of the elastic stresses, but there is cur-

rently no technique for local measurements of τ_p in a turbulent flow. On the other hand, large scale properties of the τ_p field can be inferred from measurements of the total flow resistance.

As it is well known, the high flow resistance in high Re inertial turbulence is due to large Reynolds stresses. The Reynolds stress tensor is defined by the average values of $\rho < V_i V_j >$, where V_i and V_j are different components of flow velocity. In the case of elastic turbulence the Reynolds stresses are quite small, since Re is low. Indeed, $< V_i V_j >$ can be estimated as $2V_{rms}^2$. Taking $V_{rms} = 1.55$ mm/s, which is the maximal value for RMS of the azimuthal velocity fluctuations at $r = 2d$ and $\dot{\gamma} = 4$ s $^{-1}$, we obtain a Reynolds stress of $6 \cdot 10^{-3}$ Pa, while τ_w at the same conditions is about 16 Pa. Therefore, the whole rise of flow resistance in the elastic turbulence is caused by growth of average elastic stresses [15,23]. By the same token, the irregular fluctuations of the total flow resistance in the elastic turbulence, that were discussed above (Fig.4), are due to fluctuations in the τ_p field at large spatial scales.

Average growth of the polymer stresses can be estimated from the curves in Fig.3. Indeed, by momentum conservation the stress near the wall should be equal to its average value in the bulk, $\tau_w = \tau_p + \tau_s$, $\tau_w^{lam} = \tau_p^{lam} + \tau_s^{lam}$ (we omitted signs of averaging for brevity). The viscous stress due to Newtonian solvent, τ_s , is linearly proportional to the shear rate, and its average value depends only on the boundary conditions and can not change as a result of a turbulent flow [23]. Therefore, we can take $\tau_s = \tau_s^{lam} = \frac{\eta_s}{\eta - \eta_s} \tau_p^{lam}$, where η is viscosity of the polymer solution measured in a laminar shear flow at a corresponding shear rate. Then for the ratio of the average polymer stresses in turbulent and laminar flow we obtain a relation $\frac{\tau_p}{\tau_p^{lam}} = \frac{\eta}{\eta - \eta_s} \left(\frac{\tau_w}{\tau_w^{lam}} - \frac{\eta_s}{\eta} \right)$. After plugging in numeric values from Fig.3 (curve 2) and from measurements of $\eta(\dot{\gamma})$ (Fig.2) we get ratios of $\frac{\tau_p}{\tau_p^{lam}}$ as high as 65 at high shear rates. For a set-up with larger d/R and a solution with a smaller polymer concentration the ratio of the polymer stresses in turbulent and laminar flows estimated this way reached a factor of 170 [23].

In molecular theory of polymer dynamics the tensor τ_p is found to be proportional to the polymer concentration and to the average tensor of inertia of the polymer molecules, $\tau_{p,ij} \sim k < R_i R_j >$ (where k is an elasticity coefficient, which remains constant in a linear elasticity regime). Since elastic energy density of the stretched polymer molecules is given by a quadratic form of a similar kind, one can suggest linear dependence of the elastic energy on τ_p . Therefore, the density of the elastic energy should increase in the turbulent flow by about the same factor as τ_p . The density of kinetic energy is proportional to the Reynolds stress and although it certainly increases with development of the elastic turbulence, it always remains quite small compared to the elastic energy density.

So, we can suggest that the elastic stress, τ_p , should be the object of primary importance and interest in the elasticity driven turbulent flow, and it may be appropriate to view elastic turbulence as turbulence of the τ_p field.

The growth of the elastic stresses is also an evidence of significant extension of the polymer molecules in the flow. The relation $\tau_{p,ij} \sim k < R_i R_j >$ suggests that polymer extension should grow as $\sqrt{\tau_p}$. Taken together with the data on $\frac{\tau_p}{\tau_p^{lam}}$, it implies an eight-fold stretching of the polymer molecules in the turbulent flow beyond their extension in a laminar flow with the same average shear rate. (For $\frac{\tau_p}{\tau_p^{lam}} = 170$ the corresponding extension factor is 13.) Dramatic extension of the flexible polymer molecules in the turbulent flow environment, inferred here from the bulk measurements of the flow resistance, has been recently confirmed by direct visualization of individual polymer molecules in flow [28].

Behavior of polymer molecules in chaotic and turbulent flows has been a subject of a long controversy [29], and it deserves a special discussion. Dynamics of polymer liquids have been most well studied in basic rheometric flows, such as simple shear and extension. In the former case τ_p is usually found to increase slower than linearly with the rate of deformation $\dot{\gamma}$ (shear thinning). In the latter case τ_p grows faster than linearly with the rate of deformation, $\dot{\epsilon}$, and at $\dot{\epsilon} > 1/(2\lambda)$ τ_p can grow by a few orders of magnitude as the total deformation (measured by the Henky strain, $\int \dot{\epsilon} dt$) increases. Molecular basis of this behavior, stretching and tumbling in the case of a shear flow, and a coil-stretch transition in the case of an extensional flow, has been clearly demonstrated in the recent experiments by Chu's group [17,30]. A turbulent flow involves complex three-dimensional velocity field, with a tensor of rate of deformation randomly varying in time and space. Therefore, an attempt to directly fit it into the context of rheometric flows may lead to frustration and confusion.

Being stochastic phenomena, chaotic and turbulent flows are most appropriately treated statistically. An object of particular interest for polymer dynamics is statistics of deformations of the fluid elements, in which the polymer molecules reside. Since size of the polymer molecules is almost always much smaller than the size of the smallest turbulent eddies, velocity field is smooth on the scale of the molecules. At every moment of time it is defined by some average velocity and a tensor of rate of deformation, $\vec{V}(\vec{r}) = \vec{V}_0 + \frac{\partial V_i}{\partial r_j}(\vec{r} - \vec{r}_0)$. Statistics of deformations of a fluid element can be derived from statistics of the tensor $\frac{\partial V_i}{\partial r_j}$ in the Lagrangian reference frame moving with the fluid element. The tensor $\frac{\partial V_i}{\partial r_j}$ is three-dimensional and in all non-degenerate cases it has a positive eigenvalue, corresponding to extensional flow along some axis. Rate of the extension and direction of the axis vary randomly at a time scale, connected with characteristic time of variations in the flow. A detailed

statistical analysis was first made by Lumley [31] in early 70's and was revised and refined recently [32,33]. Under quite general assumptions about statistics of $\frac{\partial V_i}{\partial r_j}$, it was shown that a fluid element, which is initially a sphere, becomes an ellipsoid with its longest axis growing in average as $a = a_0 \exp(\alpha t)$. The coefficient α is a Lyapunov exponent of divergence of two closely spaced points in the flow, and the value of α is usually on the order of $\left\langle \left(\frac{\partial V_i}{\partial r_j} \right)^2 \right\rangle^{1/2}$. A somewhat surprising conclusion of the theory is that a generic random flow is in average an extensional flow in every point, with the rate of extension $\dot{\varepsilon} = \alpha$ and unlimited Henky strain. Therefore, one should expect the polymer molecules to become strongly stretched by the random (turbulent) flow, when the Lyapunov exponent α , as given by the statistics of $\frac{\partial V_i}{\partial r_j}$, becomes larger than $1/(2\lambda)$. (More refined theory suggests that a significant fraction of the molecules should become substantially stretched even at lower α due to intermittency in the statistics [32,33].) One can see that the strong extension of the polymer molecules in the regime of elastic turbulence, taken together with the estimate $Wi' \simeq 0.8$ are in good agreement with these theoretical predictions [32,33].

Based on the discussion above, one can suggest the following scenario of development of the elastic turbulence. The polymer molecules are stretched in the primary shear flow that leads to large elastic stresses, τ_p . The elastic stresses render the primary shear flow unstable and cause an irregular secondary flow. The flow acts back on the polymer molecules stretching them further and raising the elastic stresses even more [23]. That makes the flow increasingly turbulent, until a kind of a saturated dynamic state is finally reached. This state implies some mutually consistent fields of average stresses and velocities, and their fluctuations. Those fields are connected with each other by the equation of motion and the constitutive relation.

2. Scaling with set-up size and fluid viscosity.

We explored variation of different characteristics of the elasticity induced turbulent flow with viscosity of the polymer solution and with size of the set-up. It was in sharp contradiction with the general principles of Newtonian fluid mechanics, but quite in line with the concept of viscoelastic similarity suggested for purely elastic flow transitions [13]. So, velocity required for excitation of inertial turbulence in a Newtonian fluid is proportional to viscosity of the fluid. This is connected with the fact that characteristic inertial time (viscous diffusion time), $t_{vd} = d^2/\nu$, is inversely proportional to viscosity. In contrast to it, polymer relaxation time, λ , usually grows proportionally to viscosity of the solvent

[3]. When the system gap ratio and the viscosity ratio are both kept constant, purely elastic transitions should occur at a constant Weissenberg number, $Wi = V\lambda/L$. Therefore, increase in viscosity of the solvent should lead to transition to elastic turbulence at lower velocity. In order to verify that we prepared PAAm solutions with the same η_p/η and a relaxation times larger than 3.4 s using a few other sugar syrups with higher viscosities as solvents. The transition to elastic turbulence in these solutions occurred at the same Wi , indeed, while the angular velocity of the upper plate and Reynolds number at the transition threshold were lower, scaling as $\Omega \sim 1/\eta_s$ and $Re \sim 1/\eta_s^2$, respectively. (In fact the situation was very similar to the case of purely elastic instabilities in CT flow [13].) The dependencies of τ_w/τ_w^{lam} on Wi for those solutions were close to curve 2 in Fig.3. (In order to obtain a similar dependence, though, it was important to vary the shear rate slower, in proportion with the increase in λ .) Using a very viscous sugar syrup with $\eta_s \simeq 7.2$ Pa·s, we prepared a polymer solution with a relaxation time of about 30 s, and observed a transition to elastic turbulence at $\Omega \approx 0.05 s^{-1}$ and $Re \approx 3 \cdot 10^{-3}$ [23].

Further, the viscous diffusion time, t_{vd} , is proportional to a square of the size of the system. Therefore, when size of the set-up is proportionally reduced, the linear and angular velocities required for excitation of inertial turbulence should increase as $V \sim 1/d$ and $\Omega \sim 1/d^2$, respectively. In contrast to it, polymer relaxation time, λ , does not depend on system size. Therefore, Ω (and $\dot{\gamma}$) at transition to the elastic turbulence should not depend on size of the set-up, as long as its proportions are preserved. A natural scale of stress in the purely elastic flow regime is given by η_p/λ , and it also does not depend on size of the system. (It may depend on η_p/η_s , though.) Therefore transition to the elastic turbulence is expected to occur at the same characteristic stress, and dependence of τ_w/τ_w^{lam} on Wi is supposed to be the same for all system sizes.

Figure 14 shows dependence of τ_w/τ_w^{lam} on Wi in a set-up with all the dimensions proportionally reduced by a factor of four compared with the standard configuration. The plot looks quite similar to curve 1 in Fig.3. One can see that the transition to the elastic turbulence indeed occurred at the same $\dot{\gamma}$ as in the standard set-up, although the Reynolds number was 16 times lower. In order to compensate for lower sensitivity of the rheometer to shear stress due to smaller total torque, the rate of variation of $\dot{\gamma}$ was reduced. That may be the reason for a smaller region of hysteresis in Fig.14 compared with Fig.3. The plot in Fig.14 also implies that the transition to elastic turbulence occurred at the same τ_w and Wi , and dependence of τ_w on $\dot{\gamma}$ was also almost the same as in the standard configuration.

The parameters of the system relevant to the elastic turbulence are d , R , η_p , η_s , λ and Ω . (Density of the

fluid should be of no importance, since inertial effects are negligible.) There seems to be no apparent way to construct out of these parameters a scale of length other than the size of the system (with a possible pre-factor depending on η_p/η_s and $\Omega\lambda$). It implies that, when the dimensions of the system, d and R , are proportionally changed, while η_p , η_s , λ and Ω are preserved, the turbulent velocity field should remain the same up to linear rescaling with size of the system.

This suggestion is qualitatively confirmed by the mixing patterns presented in Fig.15. The snapshots in the left column are the same as in Fig.9. They show consecutive stages of mixing of a droplet of ink in a polymer solution upon sudden inception of shear flow. The dimensions of the system were two times smaller than those of the standard configuration. The snapshots in the right column show mixing in the same polymer solution in a system with dimensions reduced four-fold compared with the standard configuration. In both cases the area of the snapshots corresponds to the area of the upper plates. So, the snapshots in the right column are magnified by a factor of two compared with the snapshots in the left column. (The volume of the ink droplet added to the solution in the right column was 4 times smaller than for the left column in order to match the amount of ink per unit area.) The angular velocities of the upper plates were the same, $\Omega = 1.5 \text{ s}^{-1}$, and so were the shear rates, $\dot{\gamma} = 5.6 \text{ s}^{-1}$, and the Weissenberg numbers. However, the Reynolds number for the right column was four times smaller, $Re = 0.125$ compared with $Re = 0.5$ for the left column.

The mixing patterns in Fig.15 are irregular in the both columns, but the two sequences look rather similar and make an impression of two realizations of the same stochastic process. So the transition to the elastic turbulence seems to go similarly in the two systems, and the mixing seems to progress with about the same characteristic time. This implies that characteristic velocities of the irregular flow scale linearly with size of the system and with velocity of the primary flow. Patterns, which appear in the snapshots taken at equal elapsed times, seem to have similar sizes and similar contrast levels. This suggests that in the elastic turbulence characteristic spatial scales of velocity field are indeed proportional to size of the system.

Quantitative data on dependence of the turbulent velocity field on the system size are obtained from velocity spectra measured at a point with a large mean flow velocity. As it was argued above, those measurements provide information about both power of the velocity fluctuations and spatial structure of the velocity field. Spectra of fluctuations of the azimuthal and radial velocity components measured at $r = 2d$, $z = d/4$ in the standard and in the half-size set-ups are shown in Fig.16. The shear rate was 4 s^{-1} (corresponding to $Wi = 13.5$) in the both systems, the same as for the spectra in Fig.8 and for PDF's in

Figs.12,13.

From the above similarity arguments fluctuating velocity was expected to scale as d/λ . RMS of the fluctuations of V_ϕ and V_r were 1.55 mm/s and 0.97 mm/s, respectively, for the standard configuration, and 0.78 mm/s and 0.48 mm/s, respectively, for the half-size system. So the corresponding fluctuation amplitudes in the half-size system were indeed twice lower. Therefore, in order to match spectra in the two systems, the velocity measured in the half-size system was multiplied by a factor of 2. One can see, that upon this velocity rescaling, the spectra of both V_ϕ and V_r become very close. The apparent difference at high frequency is due to lower signal-to-noise ratio in the half-size system. Indeed, one of the main sources of noise in the LDV measurements is finite size of the crossing region of the laser beams, over which the measured velocity is averaged. Characteristic velocity gradients (scaling with Ω and $1/\lambda$) are expected to be equal in the two systems, and dimensions of the laser beam crossing region are the same as well. Therefore, the level of the gradient noise should not change, when the size of the system is reduced, whereas the level of the signal (characteristic fluctuating velocity) decreases.

The average azimuthal velocities were 6.34 mm/s and 3.37 mm/s for the standard and the half-size systems, respectively, with their ratio being rather close to 2 again. Therefore, applying the Taylor hypothesis to the power spectra in Fig.16, we conclude that spatial structure of the velocity fluctuations in the two systems is statistically identical up to rescaling by a factor of 2 in the k -space. Thus, the experimental results in Fig.16 provide further, more quantitative support to the suggestion of simple linear rescaling of the turbulent velocity field with size of the system at constant Ω (and η_p , η_s and λ).

3. Flow at small scales and near walls.

Structure of flow at small scales and near boundaries gives another example of substantial differences between the elastic and inertial turbulence. It is instructive to summarize some relevant basic facts about the latter first. In high Re inertial turbulence the range of excited spatial scales is restricted from below by the Kolmogorov dissipation length, l_0 . It can be estimated from the condition $Re_{l_0} \simeq 1$ [1,27], with the local Reynolds number, Re_l , defined as $V_l l / \nu$, where V_l is a characteristic turbulent velocity difference at the scale l . Since V_l decreases as l becomes smaller (as $V_l \sim l^{1/3}$ in Kolmogorov's picture of turbulence [1,27]), Re_l decreases faster than linearly with decreasing l . So, the dissipation length l_0 necessarily exists in any inertial turbulent flow.

An issue related to the problem of the smallest excited length scale is stability of boundary layers near solid walls. The latter can be most simply approached by introduction of a local Reynolds number, $Re(z) =$

$\bar{V}(z)z/\nu$, which is a growing function of distance, z , from the wall. (The usual convention is to use y for distance from a wall (transverse direction), and z as a coordinate in the spanwise direction, but we would like to stay consistent with the notation used in Fig.11 and cylindrical geometry.) Near a wall the mean flow velocity, $\bar{V}(z)$, increases linearly with z , giving $Re(z) \sim z^2$ at small z . Therefore, $Re(z)$ remains low in some vicinity of a wall and the flow there is a laminar shear. This laminar shear layer near a wall (usually called viscous sublayer) ends at a distance z (decreasing with growth of global Re), where $Re(z)$ becomes sufficiently large, and the shear flow becomes unstable and turbulent.

Analogously to the inertial turbulence, we can introduce a local Weissenberg number, $Wi_l = \lambda V_l/l$. It does not decrease as l becomes smaller, though. Indeed, the ratio V_l/l is a characteristic gradient of the turbulent velocity smoothed over the length l , and it can only grow as l decreases. Since Wi_l does not get small at small l , there appears to be no straightforward way to construct an analog of the dissipation length, l_0 , for the elastic turbulence. So, there may be no macroscopic length setting a lower limit to the range of scales of the turbulent motion. (Something may change, though, at a scale comparable with size of the polymer molecules or with their characteristic diffusion length.)

This suggestion is consistent with the plots shown in Fig.16. Indeed, the spectra of both V_ϕ and V_r in Fig.16 have broad frequency ranges where the power of fluctuations decays as $P \sim f^{-\alpha}$. The value of α is close to the values found for the other velocity spectra (Fig.5, 8). The highest frequency in a power law decay region corresponds to the smallest spatial (or temporal) scale, at which the turbulent flow is excited. The power law decay regions in the spectra in Fig.16 are cut off at high frequencies by plateaus rather than by abrupt drops, however. As we argued before, those plateaus appear solely due to the instrumental noise. The power law decay range and the apparent range of excited spatial scales deduced from it become broader, when the signal-to-noise ratio becomes higher, Fig.16. This lack of the cut-off frequency from above does not lead to any kind of high frequency divergence (ultraviolet catastrophe), though. Indeed, since $\alpha > 3$, the total power of the velocity fluctuations is converging at high f and k , and the same is true for fluctuations of velocity gradients with their power scaling as $P \sim k^{-(\alpha-2)}$ in the spatial domain. (We assume again that the Taylor hypothesis is applicable.)

Similarly to $Re(z)$, one can introduce a local Weissenberg number near a wall, $Wi(z) = \lambda \bar{V}(z)/z$ ($\bar{V}(z)$ here is the difference between the local mean flow velocity and the velocity at the wall at $z = 0$), and easily see that it does not become small at $z \rightarrow 0$. In fact, we can learn from the average velocity profiles in the elastic turbulence, Fig.11, that the region near the upper plate corresponds to the highest average shear rate and to the

highest $Wi(z)$. On the other hand, the velocity fluctuations clearly decline near the upper plate, Fig.11, and existence of such a stable high shear rate boundary layer in the elastic turbulence may appear rather puzzling.

A possible mechanism providing stability of the flow near the upper plate is significant shear thinning of the relaxation time, λ . As it was argued above, in the elastic regime flow stability depends on the parameter $K = \frac{\eta_p}{\eta} \frac{d}{R} Wi^2$. Adopting it for the boundary layer, we can suggest that stability should be defined by a local parameter $K(z) = \frac{\eta_p}{\eta} \frac{z}{R} Wi^2(z)$, where $Wi(z) = \lambda(\dot{\gamma}) \bar{V}(z)/z$, $\lambda(\dot{\gamma})$ is the shear rate dependent relaxation time, and R is the radial position of the region of interest. We can consider a case of a simple sigmoidal profile, where the whole growth of the mean flow velocity from zero to \bar{V} occurs across thin layers of widths z_b near the boundaries. If \bar{V} , $\frac{\eta_p}{\eta}$, and R are all kept constant, we obtain $K(z_b) \sim \lambda^2(\dot{\gamma})/z_b$, where $\dot{\gamma} = \bar{V}/z_b$. Therefore, if the relaxation time decreases with the shear rate faster than $\lambda \sim \dot{\gamma}^{-1/2}$, $K(z_b)$ is a decreasing function, and the boundary layer remains stable as it becomes thinner and the slope, \bar{V}/z_b , increases.

Such fast decay of λ with $\dot{\gamma}$ would also suggest that a more global (although radius dependent) parameter for the flow between two plates $K = \frac{\eta_p}{\eta} \frac{d}{R} [\lambda(\frac{\Omega R}{d}) \frac{\Omega R}{d}]^2$ would be decreasing with R , and the elastic instability would be limited to a region of sufficiently small R . This kind of behavior was indeed reported for a different polymer solution and a system with small d/R [20]. In a more general case of shear thinning, with the relaxation time scaling as $\lambda = \lambda_0 \dot{\gamma}^{-\alpha}$ (and $\alpha < 1/2$), the condition $K < K_c$ (where K_c is a critical value for instability) is satisfied for $\bar{V}(z) < \left[\frac{K_c \eta R}{\eta_p \lambda_0^\alpha} \right]^{1/(2-2\alpha)} \cdot z^{\frac{1-2\alpha}{2-2\alpha}}$, which is reminiscent of the $\bar{V}(z)$ profiles in Fig.11.

Dependence of λ on $\dot{\gamma}$ in a shear flow can be inferred from measurements of normal stress difference, N_1 . At $\lambda \dot{\gamma} \ll 1$ it is usually found that $N_1 = 2\lambda \eta_p \dot{\gamma}^2$ with constant λ and η_p . Therefore, $\lambda(\dot{\gamma}) = N_1/(2\eta_p \dot{\gamma}^2)$ can be used as an estimate of shear thinned relaxation time at higher $\dot{\gamma}$. Measuring this way $\lambda(\dot{\gamma})$ for solutions of a few lower molecular weight PAAm samples we usually found $\lambda \sim \dot{\gamma}^{-\alpha}$, with α around 0.3 [12]. (Resolution of our rheometer was not sufficient to measure normal stresses in the solution used in the experiments on the elastic turbulence at Wi in the range of interest [12].) Therefore the shear thinning may indeed play an important role in stabilization of the boundary layer.

Finally, it is worth noting that the whole concept of boundary layers is less straightforward in the case of elastic turbulence, and the condition of their stability may be less restrictive than for inertial turbulence. Indeed, in a high Re turbulent flow characteristic fluctuating velocity, $V'(z)$, generated by a flow instability originating at a distance z from a wall scales as $V'(z) \sim \nu/z$, and

the boundary layer must become stable at some z , since $V'(z) \rightarrow \infty$ as $z \rightarrow 0$. In contrast, characteristic fluctuating velocity generated by an elastic instability should be proportional to z/λ and approaching zero at $z \rightarrow 0$.

IV. COUETTE-TAYLOR FLOW.

A. Experimental set-up and results.

The experiments on the Couette-Taylor flow were carried out in a small set-up mounted vertically on the AR-1000 rheometer. The stationary outer cylinder was made of glass, had a radius $R_2 = 13.5$ mm, was open from above and closed from below by a stainless steel plug with a flat top, Fig.17. The rotating inner cylinder had a radius $R_1 = 9$ mm and was conical at the bottom with an angle of $\tan^{-1}(0.5)$, so that the gap ratio in the cone-and-plate flow at the bottom was the same as in the annular gap, $d/R_1 \equiv (R_2 - R_1)/R_1 = 0.5$. The cylindrical surface of the inner cylinder was 72 mm long. The both cylinders were coaxial with the shaft of the rheometer, and the inner cylinder was attached to it. The working liquid was filled above the upper rim of the inner cylinder. In order to reduce evaporation of the fluid from its open surface a special cover (vapor trap) was used. The outer cylinder was enclosed in a thermal jacket with a square cross-section that was made out of plexiglass. The temperature of the system was set by a fast stream of water pumped through the jacket from a refrigerated circulating bath. The polymer solution was the same as in the experiments on the flow between two plates (80 ppm of PAAm in 65% sucrose, 1% NaCl in water), and the experiments were carried out at the same temperature of 12 °C. The characteristic shear rate in the flow was calculated as $\dot{\gamma} = \Omega R_1/d$, and the Weissenberg number was taken to be $Wi = \lambda \Omega R_1/d$ with $\lambda = 3.4$ s.

First, we measured flow resistance in the polymer solution as a function of $\dot{\gamma}$ and Wi . The protocol was very similar to that described above for the flow between two plates. At the beginning, pure solvent (with a viscosity η_s) was filled into the system and torque, T_s , applied to the inner cylinder was measured as a function of angular velocity, Ω . The dependence was linear over the whole range of Ω explored. Suggested dependence of torque for an (imaginary) laminar flow of the polymer solution was calculated from it as $T_{lam} = T_s \eta(\dot{\gamma})/\eta_s$. Then the system was filled with the polymer solution, Ω was gradually increased starting from a low point corresponding to $Wi = 0.68$, and the torque, T , required to drive the actual polymer solution flow was measured. The ratio of the two torques, T/T_{lam} , is equal to the ratio of the average stresses, τ/τ_{lam} , in the actual and the imaginary laminar flow of the polymer solution. It is a quantitative expression of growth of the flow resistance compared with the laminar flow. The dependence of τ/τ_{lam} on Wi

is shown in Fig.18 (thin black line) for Wi varying over almost two orders of magnitude. One can see that the resistance ratio τ/τ_{lam} is equal to unity at low values of Wi corresponding to laminar flow in the system. Then at Wi of about 4 an abrupt transition occurs, and the flow resistance starts growing quickly and non-linearly. Reynolds number at the transition point is quite small, $Re = \Omega R_1 d \rho / \eta = 0.07$. Therefore, the transition is of a purely elastic nature. The non-linear growth of the flow resistance is quite significant; at the highest tested value of Wi the ratio τ/τ_{lam} is more than 4. Undulations of the curve in Fig.18 reflect fluctuating nature of the flow resistance above the transition and are due to limited integration time during the measurements.

In order to explore behavior of the flow resistance at decreasing shear rate, we carried out another experiment, where Wi was first set to 7, well above the transition point, and gradually reduced afterwards. Dependence of τ/τ_{lam} on Wi in this run is shown by a thick gray curve in Fig.18. The two curves in Fig.18 overlap at Wi above 4.7 and below 1.8, whereas in the region in between a well pronounced hysteresis occurs. This broad region of hysteresis agrees quite well with previously reported results for Couette-Taylor flow in a purely elastic regime, which were obtained in a system with a smaller gap ratio and a different PAAm solution [12,13]. The appearance of the plot in Fig.18 is quite similar to the dependencies of τ/τ_{lam} on Wi for the flow between two plates shown in Figs.3 and 14.

The non-linear velocity transition was accompanied by emergence of a disordered and randomly fluctuating pattern of vortices on top of the basic shear flow. When visualized with the light reflecting Kalliroscope flakes, the fluctuating pattern looked similar to the Disordered oscillations reported before at similar flow conditions in a larger CT system with $d/R_1 = 0.2$ [12]. In order to measure velocity associated with the fluctuating flow we used the LDV set-up again. Two horizontal laser beams were crossing inside the polymer solution seeded with polystyrene beads in the middle of the annular gap at $r = (R_1 + R_2)/2$ and at about half height from the bottom. The beams were adjusted in such a way that it was the radial component of the flow velocity, V_r , perpendicular to the basic shear flow that was measured. Power spectra of fluctuations of V_r at a few different Wi above the non-linear transition are shown in Fig.19. As Wi is raised the total power of the velocity fluctuations increases and fluctuations at higher frequencies are excited. Nevertheless, all four curves share the same general appearance: there are two plateau regions at low and high f (the latter should be due to the instrumental noise) and two contiguous regions of a power law decay in between, with two different exponents and a distinct inflection point separating them. Although characteristic frequencies increase with Wi , those exponents are rather

close for all four curves, around -1.1 at lower frequencies and around -2.2 in the high frequency power law decay regions. Apart from the inflection points, none of the curves exhibits any distinct peaks. Amplitude of the velocity fluctuations in all four cases was quite small compared with average flow velocity. The latter was directed along the circumference (azimuthally) and equal to about $\Omega R_1/2$. (See also Fig.20 below and discussion thereof). Therefore, the spectra in Fig.19 should actually reflect spatial variation of V_r in the azimuthal direction.

In order to obtain additional information about the fluctuating flow velocity, we used the same time series to calculate velocity statistics. The probability distribution functions of V_r at different Wi are shown in Fig.20. One immediately observes that, although the average velocity is always zero, the shapes of the distributions are essentially non-Gaussian. Moreover, unlike the velocity distributions for the flow between two plates in Fig.12, PDF's in Fig.20 cannot be satisfactorily fitted by skewed Gaussians (functions of the form $A \cdot \exp[-(V - \bar{V}_r)^2/(2a^2) + b(V - \bar{V}_r)^3/a^3]$). One of the most notable features of the PDF's in Fig.20 is relatively high probability for large negative values of V_r ("long tails" of the distributions at negative V_r), which implies asymmetry for radial flows inwards and outwards. Although most striking in the curve for $Wi = 5.4$, this feature is still quite well expressed at $Wi = 35$. In fact, the curve at $Wi = 5.4$ is also quite similar to a PDF of V_r reported before in the CT flow with $d/R_1 = 0.2$, Ref. [12] (Fig.12 therein), at comparable Wi in the regime of Disordered oscillations. In that latter case the asymmetry in the radial velocity distribution was due to abundance of coherent structures having a shape of couples of vortices ("diwhirls") with a narrow region of intensive radial flow inwards in the middle and slow radial flow directed outwards on the sides of a vortex couple. Such an asymmetric shape of the diwhirls is closely related to mechanism of generation of the elastic instability in CT flow, and it allows efficient pumping of energy from the primary shear flow into the secondary fluctuating velocity field [12]. Therefore, the asymmetric shapes of PDF's in Fig.20 suggest that the coherent structures of that diwhirl type are present in the CT flow even at high Wi and may have significant influence on its organization and statistical properties.

The distribution functions in Fig.20 also allow finding characteristic rates of extension in the flow in the radial direction, $\partial V_r / \partial r$, and Weissenberg numbers, $Wi' = \lambda \partial V_r / \partial r$, associated with them. Indeed, we have got boundary conditions of $V_r = 0$ and $\partial V_r / \partial r = 0$ at $r = R_1$ and $r = R_2$. Therefore, $\partial V_r / \partial r$ in the bulk can be estimated as $4V_r^{rms}/d$, where V_r^{rms} is RMS of the radial velocity fluctuations. The resulting values of $\partial V_r / \partial r$ calculated from PDF's in Fig.20 are then 0.059, 0.071, 0.097 and 0.15 s^{-1} at Wi of 5.4, 13.6, 21.8 and 35, respectively. Those values of $\partial V_r / \partial r$ correspond to Wi' of 0.2, 0.24,

0.33 and 0.52, respectively. These estimated numbers are rather high and are generally consistent with the picture of strong elongation of the polymer molecules by elements of extensional flow in the fluctuating velocity field [28,31–33].

B. Discussion and comparison with the flow between two plates.

Summarizing the results shown in Figs.18-20, we conclude that in the purely elastic regime the CT flow behaves similarly to the flow between two plates described in section III. The purely elastic non-linear flow transition occurs at $Wi = O(1)$ and (arbitrarily) small Re in the both cases; the transition is rather sharp, has pronounced hysteresis and it is accompanied by significant growth of flow resistance. The fluctuating velocity field above the transition is quite random for the both flows and its spectra do not exhibit any distinct peaks, cf. Fig.8 and Fig.19. Therefore, although characterized much less extensively, the CT flow above the non-linear transition fits quite well the definition of elastic turbulence introduced above.

Nevertheless, the elasticity induced turbulent flow in the CT system differed from the turbulent flow between two plates quantitatively, and the turbulent flow effects in the CT system were less dramatic. Indeed, the non-linear transition in the CT system occurred at $Wi \approx 4$ (Fig.18), which is higher than critical Wi in the flow between two plates, 3.2 and 2, for $d/R = 0.26$ and 0.52, respectively (Fig.3). The growth of flow resistance in the CT flow above the transition was notably smaller than in the flow between two plates - factor of 4.2 (Fig.18) vs. factors of 11 and 19 (Fig.3) at the highest Wi explored. (The ratio τ/τ_{lam} in the CT flow kept growing with Wi , though, and it was the increasingly fast mechanical degradation of the polymers that prevented us from raising Wi higher, Fig.18.) Characteristic amplitudes of fluctuating velocity in the CT flow (Fig.19) were significantly smaller than in the flow between two plates (Figs.11, 12), both in terms of d/λ (0.06 vs. 0.5 at $Wi \simeq 13$) and of the maximal azimuthal flow velocity (0.005 vs. 0.075 at $Wi \simeq 13$). This comparison is certainly not quite fair, since V_r in the CT flow is a transversal velocity component. Hence, it should be best compared with V_z in the flow between two plates, that was not measured. The general tendency appears to be rather clear, though.

Characteristic estimated rate of extension due to the fluctuating velocity field in the CT flow was also considerably smaller than in the flow between two plates, $0.24/\lambda$ vs. $0.83/\lambda$ at $Wi \simeq 13$. (We note here again, though, that these estimates were obtained from different types of data sets, Fig.20 vs. Fig.13). Nevertheless, even the relatively low value of the rate of extension in the CT flow is reasonably consistent with the general condition for it

to be on the order of $1/\lambda$ to cause significant elongation of the polymer molecules, growth of the elastic stresses and notable flow resistance increase.

As it was already suggested above, more favorable conditions for development of the elastic turbulence and stronger turbulent effects in the flow between two plates may be due to the large toroidal vortex. This vortex, which is driven by the distribution of normal stresses in the basic shear flow, may provide a major channel for pumping of energy into the turbulent velocity field. CT flow certainly has a more limiting geometry, without any coherent three-dimensional large scale flow of comparable magnitude and with fluid motion confined to the annular gap. That latter confinement limits possible curvature of flow trajectories and may also make the general requirement of axial symmetry for excited vortex structures (as dictated by the system geometry) more severe and restrictive, somewhat impeding development of the turbulence. In fact, axial symmetry of the vortex patterns is a quite pronounced feature in inertial turbulence in CT flow even at very high Re [34].

Among all the discrepancies between the elastic turbulence in the CT system and in the flow between two plates, the most principal one appears to be the difference in the decay exponents in the power spectra of velocity fluctuations, cf. Figs.5, 8, 16 vs. Fig.19. In the case of the flow between two plates the decay exponents were around -3.5 in the both spatial and temporal domains, while the power spectra in the CT flow had two distinct power law decay regions with significantly lower exponents of -1.1 and -2.2. As it is shown in Section V below (Fig.25), velocity spectra in an elastic turbulent flow in a curvilinear channel have regions of a power law decay as well. The decay exponents are about -3.3, suggesting that it is the CT flow that behaves "abnormally".

A clue to the behavior of the CT flow may be the inflection points in the spectra in Fig.19, which appear at frequencies $f_c = (0.45 \pm 0.05)\Omega/(2\pi)$ at all four Wi . These frequencies are close to average rates of rotation (in revolutions per second) of the fluid in the measurement point. Together with the non-Gaussian and asymmetric shapes of PDF's in Fig.20, that brings us to a suggestion that the power spectra in Fig.19 are significantly influenced by the axisymmetric coherent structures (possibly of the diwhirl type) discussed above. Those coherent structures may dominate the low frequency part of the spectra, $f < f_c$, and also feed into the high frequency part, $f > f_c$, (where the "original" power of fluctuations should be rather low to begin with, Figs.8, 16) reducing the apparent absolute values of the decay exponents at $f > f_c$.

V. FLOW IN A CURVILINEAR CHANNEL.

A. Experimental set-up and procedure.

The main motivation of the experiments on flow in a curvilinear channel (Dean flow) was to carry out detailed quantitative study of mixing in the elastic turbulence [35]. It is an open flow that allows extended continuous experimental runs with reproducible and well controlled initial conditions, and easy gathering of extensive data at different stages of mixing. The channel is schematically shown in Fig.21. It had a uniform depth $d = 3$ mm, was machined in a transparent bar of perspex, and it was sealed from above by a transparent window. The channel consisted of a sequence of smoothly connected half-rings with the inner and outer radii $R_1 = 3$ mm and $R_2 = 6$ mm, respectively; it was square in its cross-section, and had quite a high gap ratio, $d/R_1 = 1$. The high gap ratio was intended to facilitate development of an elastic instability at low Wi and of intensive irregular flow above the instability threshold. The channel had 30 repeating units, 18 mm in length each, Fig.21.

The liquids to be mixed were fed into the channel by two identical syringe pumps through two separate tubing lines, always at equal discharge rates. Chemical composition of the two liquids was always identical as well, with the only difference of a small concentration, $c_0 = 2$ ppm, of a fluorescent dye (fluorescein) added to one of them. They were prepared from the same stock of a carefully filtered liquid, which was divided into two equal parts. A small amount of a concentrated solution of the dye was added to one part, while the other part was diluted by an equal amount of pure water. (Each of the liquids was carefully mixed afterwards.) This method of preparation provided very good matching of densities and refraction indices of the liquids. The channel was illuminated from a side by an Argon-Ion laser beam converted by two cylindrical lenses to a broad sheet of light with a thickness of about $40 \mu\text{m}$ in the region of observation. It produced a thin cut of the three-dimensional mixing pattern, parallel to the top and the bottom of the channel at a half of the channel depth.

Fluorescent light emitted by the liquid in the direction perpendicular to the beam and to the channel plane was projected onto a CCD array by a camera lens and digitized by a 8-bit, 512×512 frame grabber. Using homogeneous solutions with different amounts of the dye, we found intensity of the fluorescent light captured by the camera to be linearly proportional to the dye concentration. Therefore, concentration of the dye was evaluated from the fluorescent light intensity. (The liquid without the dye appeared completely dark, Fig. 22, and signal form it was below noise level of the camera.)

The flow was always observed near the middle of a half-ring on the side, from which the laser beam was coming.

So, the number, N , of a unit (Fig.21) counted from the inlet was a natural linear coordinate along the channel. Since the total rate of liquid discharge, Q , was constant, N was also proportional to the average time of mixing. In order to observe further stages of mixing (corresponding to $N > 30$), we carried out a series of experiments, where the liquids were pre-mixed before they entered the channel. A shorter channel of the same shape was designed for this purpose and put before the entrance to the original one. In multiple calibration experiments we found good matching between states of mixing at $N = 2$ with the pre-mixer and at $N = 27$ without it [35]. Therefore, for the experiments with the pre-mixing a number of 25 was added to the actual coordinate along the channel to calculate the effective N .

Flow velocity was measured directly with the aid of the LDV set-up. Because of small width of the channel, a special effort was made to obtain high spatial resolution by reduction of the region of space, where the two laser beams crossed, and reduction of distance between the interference fringes. Focusing lenses with a small focal length (about 25 mm) were used, and the angle between the beams was raised to about 90° in the air (and about 60° in the liquid). As a result, the region of the beam crossing was brought down to $15 \times 15 \times 40 \mu\text{m}$, and the distance between the fringes was $0.44 \mu\text{m}$.

We used the same polymer solution as in the experiments on the flow between two plates and on the CT flow. (It was 80 ppm of PAAm, 65% sugar, 1% NaCl in water.) This time, however, the experiments were made at room temperature, $22.5 \pm 0.5^\circ\text{C}$. So, the solvent viscosity was $\eta_s = 0.153 \text{ Pa} \cdot \text{s}$, and viscosity of the solution was $\eta = 0.198 \text{ Pa} \cdot \text{s}$ at a shear rate $\dot{\gamma} = 4 \text{ s}^{-1}$. The relaxation time, λ , estimated from phase shift between the stress and the shear rate in oscillatory tests with a shear rate amplitude of 3 s^{-1} , was 1.4 s. An estimate for the diffusion coefficient of the dye was given by that for the saccharose molecules, $D = 8.5 \cdot 10^{-7} \text{ cm}^2/\text{s}$. The characteristic shear rate and the Weissenberg number in the flow were estimated as $\dot{\gamma} = (2Q/d^2)/(d/2) = 4Q/d^3$ and $Wi = \lambda(4Q/d^3)$, respectively. The Reynolds number was calculated as $Re = 2Q\rho/(d\eta)$.

B. Results.

The Reynolds number in the flow was always quite small, reaching only 0.6 for the highest Q that we explored. Therefore, flow of the pure solvent always remained laminar and no mixing occurred, Fig.22a. The boundary separating the liquid with and without the dye was smooth and parallel to direction of the flow and only became somewhat smeared due to molecular diffusion as the liquid advanced downstream. Flow of the polymer solution was laminar and stationary up to a value of Q corresponding to $Wi_c = 3.2$ (and $Re = 0.06$), at which

an elastic instability occurred. This instability lead to irregular flow and fast mixing of the liquids.

A few typical mixing patterns at different N in the polymer solution above the instability threshold are shown in photographs in Fig.22b-d. More insight about structure and evolution of the mixing patterns can be obtained from space-time diagrams. Representative diagrams taken at $Wi = 6.7$ at four different N are shown in Fig.23. Brightness profiles along a single line going perpendicularly to the channel near the middle of a half-ring (a horizontal line going through the middle of a snapshot in Fig.22) were captured at even time intervals of 80 ms and plotted from top to bottom. The diagrams in Fig.23 share the same chaotic appearance and show features at comparable scales, but they loose contrast as liquid advances downstream and gets progressively mixed.

As it is illustrated by the space-time diagrams in Fig.23, mixing in the polymer solution flow above the instability threshold was a random process calling for statistical analysis [35]. A simple parameter characterizing homogeneity of the mixture is a root mean square of deviations of the dye concentration from its average value, $\bar{c} = c_0/2$, divided by the average value itself, $c_{rms} = \sqrt{\langle (c - \bar{c})^2 \rangle / \bar{c}}$. Small value of c_{rms} means high homogeneity and good mixing of the liquids. At the channel entrance, where the two injected liquids are perfectly separated, c_{rms} is unity, and it should become zero for a perfectly mixed liquid.

Dependence of c_{rms} on Wi near the exit of the channel, at $N = 29$, is presented in Fig.24. Statistics of the dye concentration was evaluated from space-time diagrams similar to those in Fig.23. The regions near the walls of the channel with the widths of $0.1d$ were excluded from the statistics, though, because of possible image aberrations. In a stationary flow regime (Wi below 3.2), when the concentration profile did not change in time, the brightness profiles were measured over short time intervals (about 100 s). In the regime of an irregular flow, however, the profile of concentration was strongly fluctuating. So, in order to obtain representative statistics of c , the measurements of the brightness profile were taken during quite long intervals of time (about 20-30 min), that typically corresponded to the total liquid discharge of about $10^3 d^3$.

The plot in Fig.24 is somewhat analogous to those in Fig.3 and in Fig.18, which show dependence of the flow resistance on Wi . Indeed, the decrease in c_{rms} is an integral result of mass transfer produced by the irregular flow in the channel, just as growth of the flow resistance is an integral characteristic of increase of momentum transfer in the elastic turbulence. At Wi below 2 dye distribution patterns in the polymer solution were similar to those in the solvent, Fig.22a, with c_{rms} close to unity. Some decrease in c_{rms} at low Wi is due to large residence time and diffusional smearing of the boundary between the liquids.

At Wi of about 2 reduction of c_{rms} from 1 to about 0.9 occurred, which was a result of a transition in the flow. Although this transition produced rather complex spatial distribution of the dye (data not shown), the patterns were stationary and mixing was rather minor. This transition was probably corresponding to onset of stationary vortices with vorticity directed along the mean flow, as it was predicted in Ref. [36]. Those vortices have recently been observed directly using particle image velocimetry [37] (see also below). The most striking feature of the plot in Fig.24 is certainly an abrupt drop in c_{rms} at $Wi_c = 3.2$, where the irregular motion of the liquid set in. It is worth noting here that since the mixing and reduction in c_{rms} is a cumulative effect of stirring and diffusion in the flow starting from the inlet, the actual value of c_{rms} above the transition is defined by the distance from the inlet. On the other hand, the onset of the fluctuating flow occurred rather consistently along the whole channel, and we expect Wi_c to be virtually independent of the channel length, when the latter is sufficiently large.

We studied dependence of c_{rms} on N at $Wi = 6.7$, corresponding to highest homogeneity of the mixture near the channel exit (Fig.24), and found c_{rms} to decay exponentially with the distance from the inlet with a characteristic decay length ΔN of about 15 segments [35]. One can learn from Fig.24 that, if Wi is raised above 6.7, c_{rms} starts to increase again. The most plausible explanation for this is saturation of growth of the velocity fluctuations together with reduction of the residence time in the flow at growing Wi (and average flow velocity, $\bar{V} = Q/d^2$). If the ratio between fluctuating and average flow velocities remains constant, while they both increase, the stirring in the flow remains the same, but there is less time available for molecular diffusion, and homogeneity is reduced as a result of it. This situation can be qualitatively described by growth of the Peclet number, $Pe = \bar{V}d/D$. It was recently found for a flow of a polymer solution in a channel of the same shape and at similar Wi , that the characteristic length ΔN increases as $Pe^{0.25}$ [38]. This suggests that c_{rms} should start increasing with Wi once growth of the velocity fluctuations is slowed down.

Typical time of mixing in the channel at $Wi = 6.7$ was found to be 3-4 orders of magnitude shorter than diffusion time, d^2/D , for the small molecules of fluorescein [35]. Dependence of the efficiency of mixing at the optimal flow conditions (for the 80 ppm solution it was $Wi = 6.7$, Fig.24) on concentration of the polymers was surprisingly weak (although Wi_c grew fast, as the polymer concentration was decreasing). So, for a solution with the polymer concentration of 10 ppm ($\eta/\eta_s = 1.03$), c_{rms} of as low as 0.29 could be reached at $N = 29$. (It was measured at $Re = 0.065$, where inertial effects were still negligible). Excitation of irregular flow and active mixing was observed down to the polymer concentration of 7 ppm.

Fig.25 shows power spectra of fluctuations of longitudinal and transversal components of the velocity in the polymer solution at $Wi = 6.7$. The measurements were done at $N = 12$, near the middle of the half-ring in the middle of the channel. A spectrum of the velocity fluctuations in the flow of the pure solvent at the same Q , giving just instrumental noise, is shown for comparison. The mean velocity was $\bar{V} = 6.6 \text{ mm/s}$; the RMS of fluctuations, V_{rms} , was $0.09\bar{V}$ and $0.04\bar{V}$ in the longitudinal and transversal directions, respectively. Measuring the transversal velocity component in a few off-center positions, we found non-zero averages, which typically persisted for a few minutes and changed their sign rather randomly in time. This situation can be explained by the presence of persistent longitudinal vortical structures in the flow. These vortices should be filling the whole channel cross-section, with their vorticity direction randomly jumping between parallel and anti-parallel to the mean flow. Those vortices may first appear at $Wi = 2$ but remain stationary below $Wi_c = 3.2$.

In order to measure resistance as a function of the flow rate, we used a micro-fabricated channel with the same proportions but with a 30 times smaller segment size [39]. It had $d = 100 \mu\text{m}$, $R_1 = 100 \mu\text{m}$, $R_2 = 200 \mu\text{m}$ and consisted of 46 segments. The polymer solution had the same concentration of 80 ppm by weight of the same PAAm sample. The Newtonian solvent was significantly thinner, though, containing 35% of sucrose and 1% NaCl, and having viscosity of $4.2 \cdot 10^{-3} \text{ Pa} \cdot \text{s}$ at room temperature of 22 °C. The polymer solution viscosity was $\eta = 5.6 \cdot 10^{-3} \text{ Pa} \cdot \text{s}$ at $\dot{\gamma} = 50 \text{ s}^{-1}$.

The flow was driven by a difference of hydrostatic pressures, ΔP , applied between the inlet and outlet. Dependence of the flow rate, Q , on ΔP was measured using an in-situ compensation technique [40] (see details in Ref. [39]). Fig.26 shows resistance ratio $\Delta P/\Delta P_{lam}$ as a function of Q , where ΔP_{lam} is the pressure difference expected in a laminar flow for a liquid with a viscosity, $\eta(\dot{\gamma})$, at the same Q . (Average $\eta(\dot{\gamma})$ was calculated as $4Q/d^3$ again.) One can see a distinct transition and an onset of non-linear growth of the flow resistance at $Q \approx 8.5 \text{ nl/s}$, corresponding to $\dot{\gamma} = 34 \text{ s}^{-1}$ and $Re \approx 0.017$. The low value of Re suggests that the transition is of a purely elastic nature. Relaxation time, λ , of the polymer solution was low and could not be measured directly. For a purpose of estimation we can assume $\lambda \sim \eta_s$ and plug into this relation the values for the more viscous solution used in the table-top channel, $\lambda = 1.4 \text{ s}$ at $\eta_s = 0.153 \text{ Pa} \cdot \text{s}$. That gives $\lambda = 0.04 \text{ s}$ and $Wi = 1.3$ at the instability threshold for the current solution, which is in reasonable agreement with the results in Fig.24. As Q increases to 60 nl/s (corresponding to $Wi \approx 9$), the flow resistance growth reaches a factor of 2.8, which is comparable with the CT flow, although significantly lower than in the flow between two plates.

C. Discussion

The experimental results in Fig.24 and Fig.26 show that above the elastic instability threshold the flow of the polymer solution in the channel exhibits two major features of turbulent flows: major increase in the rate of mixing and in the flow resistance. Further, more solid evidence for the turbulent character of the flow is given by the power spectra of fluctuating velocity in Fig.25. The spectra of the both longitudinal and transversal velocity components do not exhibit any distinct peaks and have broad regions of a power law decay with a power of about -3.3. Since the power spectra in Fig.25 were measured in a point with a high mean flow velocity (10 times higher than a characteristic fluctuating velocity), we can use the Taylor hypothesis and argue that the spectra in Fig.25 actually reflect spatial structure of the flow. Then the power law decay region can be transferred to the spatial domain, with the power of the velocity fluctuations scaling as $P \sim k^{-3.3}$ with the wave number, k . The absence of peaks in the spectra in Fig.25 and significant extension of the frequency region, where P follows the power law, are strong evidence of fluid motion in a broad range of spatial scales and of turbulent character of the flow. We also notice here that the exponent of -3.3 in Fig.25 is very close to those measured in the flow between two plates, Figs.5, 8, 16, which varied from -3.3 to -3.6 depending on the position. So, one can suggest that decay of the power of the velocity fluctuations with an exponent around -3.5 is a rather general feature of the elasticity induced turbulent flows. It does not appear in the radial velocity spectrum of the CT flow (Fig. 19), though, possibly because of abundance of the coherent axisymmetric structures (see Section 4B).

The functional form of the velocity power spectra, $P \sim k^{-3.3}$, deduced from Fig.25, suggests that the power of fluctuations of velocity gradients scales as $k^{-1.3}$. An integral of $k^{-1.3}$ diverges at $k \rightarrow 0$ and converges at $k \rightarrow \infty$. It means that the main contribution to the fluctuations of the velocity gradients and the velocity differences at all scales comes from the biggest eddies, having dimensions of the whole system (diameter of the channel). This conclusion has an immediate implication for mixing in the flow: it should result in the same type of patterns and in functionally the same statistics as in the case of a completely homogeneous flow, $\vec{V}(\vec{r}, t) = \vec{V}_0(t) + \frac{\partial V_i}{\partial r_j}(t) \cdot (\vec{r} - \vec{r}_0)$, randomly varying in time.

Such a flow is a realization of the so-called Batchelor regime of mixing [41], and the problem of statistics of a tracer (dye) distribution in it has been solved analytically recently [42–44]. The Batchelor regime occurs at small scales (below the Kolmogorov dissipation scale [1,27]) in the usual, high Re , turbulence, and it is rather difficult to realize in laboratory otherwise. Therefore, the elastic

turbulent flow in the channel provided a very convenient experimental system for quantitative study of mixing in this regime [35]. The experimental results on correlation functions and PDF of dye concentration, and on their dependence on time of mixing agreed very well with the theoretical predictions [35]. A practical message of the experiments is that very viscous liquids can be efficiently mixed in curvilinear channels at very low flow rates by adding high molecular weight polymers at very low concentrations. This method of mixing, we believe, can find some industrial and laboratory applications [45].

VI. CONCLUDING REMARKS.

We studied flows of dilute solutions of a flexible high molecular weight polymer in three different flow set-ups, which shared the same feature of high curvature of the flow lines, quantitatively expressed in large gap ratios, d/R . High viscosity of the solvent and long polymer relaxation times ensured an elasticity dominated flow regime, where effects of the non-linear constitutive relation between polymer stress and rate of deformation prevailed over the inertia related non-linearity of the Navier-Stokes equation. As a result, all flow transitions were induced by the non-linear elasticity, occurred at Wi on the order of unity and at very low Re . In all three systems, a flow above the instability threshold was randomly fluctuating in time and space, and exhibited some or all of the main features of turbulence: fluid motion excited in a broad range of spatial and temporal scales, and significant increase in the rates of momentum and mass transfer (flow resistance and mixing). The extend of the flow resistance growth varied rather substantially between the systems (factors of 20, 4.2 and 2.8 for the flow between two plates, the CT flow, and the flow in the curvilinear channel, respectively) and so did the exponents in the power law decay regions of the velocity spectra (being from -3.3 to -3.6 for the flow between two plates, -1.1 and -2.2 for the CT flow, and -3.3 for the curvilinear channel). We believe, however, that all the experimental findings are fitting rather well to the same general framework of a phenomenon, which we call elastic turbulence.

Observation of the elastic turbulence and investigation of its properties have been greatly facilitated by the choice of the systems with large d/R , where the elastic instability occurs at low Wi , and by the choice of the high molecular weight polymer, which is only moderately extended (compared to its full contour length) at the instability threshold. Nevertheless, we believe that elements of the elastic turbulence should generally appear in three-dimensional flows of polymer solutions at high Wi and low Re . Possible realizations of this regime may range from flows of polymer melts in industrial reactors to small scale flows in drag reducing aqueous polymer solutions.

Dependence of the elastic turbulence onset conditions on parameters of the system and on properties of the polymers solution (discussed in Section III.D.2) implies that using polymer solutions with sufficiently high elasticity, one can excite turbulent motion at arbitrary low velocities and in arbitrary small tanks. (In some cases it may be the only way to produce a chaotic flow, which may be needed for fluid mixing.) Irregularly fluctuating flows showing multiple features of the elastic turbulence have been recently demonstrated in a rotating flow between two plates with a 300 μm gap [28] and in a 100 μm thick curvilinear channel [39]. An apparent restriction is, however, that the size of the tank has still to be large compared to the size of the polymer coils.

Recently there have been some serious advances in theory of random flows of polymer solutions in the regimes of both high and low Re [25,26,32,33]. In particular, the following explanation of the velocity spectra shapes in Figs.5, 8, 16, 25 was proposed [26]. Fast decay of the fluctuation power with k implies a velocity field, where the main contribution to deformation and stirring (stretching and folding) at all scales comes from randomly fluctuating velocity field at the largest scale of the system. Therefore, it is suggested that the leading mechanism for generation of small scale (high k) fluctuations in the elastic stress is advection of the fluid (which carries the stress) in this fluctuating large scale velocity field. Hence, the fluctuating velocity field and stress tensor can both be decomposed into large and small scale components, and the leading mechanism for generation of the small scale (high k) portions is advection by the fluctuating large scale flow. (The theory considers the elastic stress tensor being passively advected in a random velocity field, that is analogous to the concept of a passively advected vector in the magnetic dynamo theory [26].) The small scale velocity fluctuations are a product of the small scale stress fields. The elastic stresses are mainly pumped by the large scale flow field, and the smaller scale stress fields created by the advection are permanently decaying because of the polymer relaxation. These simultaneously occurring advection and relaxational decay of τ_p result in a quick decay of τ_p fluctuations at large k that should produce $P \sim k^{-\alpha}$ velocity spectra with $\alpha > 3$. The current understanding of the elastic turbulence is still remaining quite incomplete, however, and this phenomenon certainly awaits further detailed experiments and numerical simulations.

Acknowledgement. We are grateful to M. Chertkov, G. Falkovich, and V. Lebedev for many useful and illuminating discussions. This work is partially supported by an Israel Science Foundation grant, Binational US-Israel Foundation, and by the Minerva Center for Nonlinear Physics of Complex Systems.

A. List of notations.

- c - passive tracer (dye) concentration,
- \bar{c} - average concentration,
- c_0 - initial concentration of dye,
- c_{rms} - root mean square of deviations of dye concentration from its average divided by the average,
- d - gap width,
- d/R - gap ratio,
- f - frequency,
- k -wave number,
- $K = (d/R)(\eta_p/\eta)Wi^2$ - parameter of elastic non-linearity for normal stress driven instabilities in curvilinear flows,
- L - system size,
- M_w - average molecular weight,
- N - number of half-ring in a curvilinear channel,
- N_1 - first normal stress difference,
- p - pressure,
- P - power of fluctuations,
- Pe - Peclet number,
- Q - flow discharge rate,
- r, ϕ, z - cylindrical coordinates (radial, azimuthal, axial),
- R - radius of either a plate in rotating flow between two plates or inner cylinder in Couette-Taylor flow,
- R_g - radius of gyration of a polymer,
- $Re = VL/\nu$ -Reynolds number,
- $t_{vd} = d^2/\nu$ - viscous diffusion time,
- T - torque,
- T_{lam} - torque in polymer solution flow in a laminar regime,
- T_s - torque measured in a solvent flow,
- $Ta = (d/R)Re^2$ - Taylor number,
- V_r - radial (spanwise) velocity component, D -diffusion coefficient,
- V_ϕ - azimuthal (longitudinal) velocity component,
- Wi - Weissenberg number,
- Wi_c - critical Wi of the elastic instability onset,
- z_b - characteristic thickness of boundary layer,
- $\dot{\gamma}$ - shear rate,
- λ - polymer relaxation time,
- η - viscosity,
- η_s - viscosity of Newtonian solvent,
- η_p - part of solution viscosity due to polymer molecules,
- η' - in-phase component of viscosity in an oscillatory test,
- η'' - out-of-phase component of viscosity in an oscillatory test,
- ν - kinematic viscosity,
- ρ - density,
- τ - stress tensor,
- τ_s - stress tensor due to Newtonian solvent,
- τ_p - polymer stress tensor,
- τ_w - shear stress near a wall,

τ_w^{lam} - shear stress near a wall in a laminar flow,

Ω - rotation (angular) velocity.

- [1] L. D. Landau and E. M. Lifschitz, *Fluid Mechanics*, (Pergamon Press, Oxford), 1987.
- [2] D. J. Tritton, *Physical Fluid Dynamics*, (Clarendon Press, Oxford), 1988.
- [3] R. B. Bird, C. F. Curtiss, R. C. Armstrong, and O. Has-sager, *Dynamics of Polymeric Liquids*, (John Wiley, NY), 1987.
- [4] K. Weissenberg, *Nature* **159**, 310 (1947).
- [5] V. Tirtaatmadja and T. Sridhar, *J. Rheology* **37**, 1081 (1993).
- [6] J. J. Magda, and R. G. Larson, *J. Non-Newtonian Fluid Mech.* **30**, 1 (1988).
- [7] S. J. Muller, R. G. Larson, and E. S. G. Shaqfeh, *Rheol. Acta* **28**, 499 (1989).
- [8] D.V. Boger, *J. Non-Newtonian Fluid Mech.* **3**, 87 (1978).
- [9] R. G. Larson, E. S. G. Shaqfeh, and S. J. Muller, *J. Fluid Mech.* **218**, 573 (1990).
- [10] R. G. Larson, *Rheol. Acta* **31**, 213 (1992).
- [11] E. S. G. Shaqfeh, *Annu. Rev. Fluid Mech.* **28**, 129 (1996).
- [12] A. Groisman and V. Steinberg, *Phys. Fluids* **10**, 2451 (1998).
- [13] A. Groisman and V. Steinberg, *Europhys. Lett.* **43**, 165 (1998).
- [14] H. W. Giesekus, *Rheol. Acta* **7**, 127 (1968).
- [15] A. Groisman and V. Steinberg, *Nature* **405**, 53 (2000).
- [16] D. V. Boger, K. Walter, *Rheological phenomena in focus*, (Elsevier) (1993).
- [17] D.E. Smith, H. P. Babcock, and S. Chu, *Science* **283**, 1724 (1999).
- [18] J. A. Byars, A. Öztekin, R. A. Brown, and G. H. McKinley, *J. Fluid Mech.* **271**, 173 (1994).
- [19] M. Doi and S. F. Edwards, *The Theory of Polymer Dynamics*, (Clarendon Press, Oxford), 1988.
- [20] G. H. McKinley, J. A. Byars, R. A. Brown, and R. C. Armstrong, *J. Non-Newtonian Fluid Mech.* **40**, 201 (1991).
- [21] A. Groisman, M.Sc. Thesis, Weizmann Institute of Science, Rehovot, 1993.
- [22] *International Critical Tables*, v.5, McGraw-Hill, New York, 1929.
- [23] A. Groisman and V. Steinberg, *Phys. Rev. Lett.* **86**, 934 (2001).
- [24] J. R. Stokes, L. J. W. Graham, N. J. Lawson, and D. V. Boger, *J. Fluid Mech.* **429**, 67,117 (2001).
- [25] E. Balkovsky, A. Fouzon, and V. Lebedev, *Phys. Rev. E* **64**, 056301 (2001).
- [26] A. Fouzon and V. Lebedev, *Phys. Fluids* **15**, 2060 (2003).
- [27] U. Frish, *Turbulence: The Legacy of A. N. Kolmogorov* (Cambridge University Press, New York), 1995.
- [28] S. Geraschenko, C. Chevallard, and V. Steinberg, submitted for publication, 2003.
- [29] A. Gyr and H.-W. Bewersdorf, *Drag Reduction in Tur-*

- bulent Flows by Additives*, (Kluwer, London), 1995.
- [30] T. Perkins, D. Smith, S. Chu, *Science* **276**, 2016 (1997).
- [31] J. Lumley, *Symp. Math.* **9**, 315 (1972).
- [32] E. Balkovsky, A. Fouzon, and V. Lebedev, *Phys. Rev. Lett.* **84**, 4765 (2000).
- [33] M. Chertkov, *Phys. Rev. Lett.* **84**, 4761 (2000).
- [34] D. P. Lathrop, J. Fineberg, and H. L. Swinney, *Phys. Rev. A* **46**, 6390 (1992).
- [35] A. Groisman and V. Steinberg, *Nature* **410**, 905 (2001).
- [36] Y.L. Joo and E.S.G. Shaqfeh, *Phys. Fluids A* **3**, 1691 (1991).
- [37] T. Burghela, E. Segre, and V. Steinberg, to be published
- [38] T. Burghela, E. Segre, and V. Steinberg, nlin.CD/0401003 and submitted for publication, 2003.
- [39] T. Burghela, E. Segre, I. Bar-Joseph, A. Groisman, and V. Steinberg, nlin.CD/0312071 and submitted for publication, 2003.
- [40] A. Groisman, M. Enzelberger, and S. R. Quake, *Science* **300**, 955 (2003).
- [41] G.K. Batchelor, *J. Fluid Mech.* **5**, 113 (1959).
- [42] B.I. Shraiman and E.D. Siggia, *Nature* **405**, 639 (2000).
- [43] M. Chertkov, G. Falkovich, I. Kolokolov and V. Lebedev, *Phys. Rev. E* **51**, 5609 (1995).
- [44] E. Balkovsky and A. Fouzon, *Phys. Rev E* **60**, 4164 (1999).
- [45] V. Steinberg and A. Groisman, *Device and Method for Mixing Substances*, US Patent No. 6,632,014 B2, Oct. 14, 2003.

FIG. 1. Schematic drawing of the experimental set-up. The set-up consists of a stationary cylindrical cup with a flat bottom (the lower plate), which is concentric with the rotating upper plate. A special cover is put from above to minimize evaporation of the liquid.

FIG. 2. Upper curve: dependence of the apparent viscosity, $\eta(\dot{\gamma})$, of 80 ppm PAAm solution in 65% sucrose, 1% NaCl in water at 12 °C on shear rate (semi-logarithmic coordinates). Applied shear rate was gradually increased during the test. Lower curve shows a similar run for the pure solvent. *Inset*: apparent relaxation time, λ , as a function of angular frequency, ω , measured for shear rate oscillations with an amplitude of 1 s^{-1} .

FIG. 3. The ratio of the average stress at the upper plate, τ_w , measured in the flow, to the stress, τ_w^{lam} , in imaginary laminar shear flow with the same boundary conditions, as a function of the shear rate, $\dot{\gamma}$. The curves 1 and 2 are for the polymer solution flow with the gap $d = 10 \text{ mm}$ and 20 mm , respectively. The shear rate was gradually varied in time. Thin black lines represent increasing $\dot{\gamma}$; thick gray lines represent decreasing $\dot{\gamma}$. Curve 3 is for the pure solvent.

FIG. 4. Power spectra of fluctuations of the angular velocity, Ω , of the upper plate at different applied torques, T . Curves 1 - 5 correspond to average shear rates of 1.25, 1.85, 2.7, 4 and 5.9 s^{-1} , respectively (all above the transition point $\dot{\gamma} \simeq 1 \text{ s}^{-1}$, Fig.3). The power, P , of fluctuations is fitted by a power law, $P \sim f^{-4.3}$, for $\dot{\gamma} = 4 \text{ s}^{-1}$ over about a decade in frequencies, f . Curve 6, taken with the pure solvent at a shear rate of 4 s^{-1} , shows instrumental noise.

FIG. 5. Power spectra of velocity fluctuations in the standard set-up at different shear rates, $\dot{\gamma}$. The fluid velocity was measured by LDV in the center of the flow. The curves 1 - 5 correspond to $\dot{\gamma} = 1.25, 1.85, 2.7, 4$, and 5.9 s^{-1} , respectively (all above the transition point $\dot{\gamma} \simeq 1$, Fig.3). The power, P , of fluctuations is fitted by a power law, $P \sim f^{-3.5}$, for $\dot{\gamma} = 4 \text{ s}^{-1}$ over about a decade in frequencies, f .

FIG. 6. Representative snapshots of the flow taken from below. Field of view corresponds to the upper plate area. The flow was visualized by seeding the fluid with light reflecting flakes. (a-b) the polymer solution at $Wi = 6.5$, $Re = 0.35$; (c-e) the polymer solution at $Wi = 13$, $Re = 0.7$; (f) the pure solvent at $Re = 1$.

FIG. 7. Average Fourier spectra of the brightness profiles taken along the diameter (thin black line) and along the circumference at a radius of $2d$ (thick gray line). The averaging was made over about 20 minutes of the flow time and about 2000 snapshots.

FIG. 8. Power spectra of fluctuations of radial velocity, V_r , at $\dot{\gamma} = 4 \text{ s}^{-1}$ measured at $z/d = 0.5$ at different radii. Curves 1 - 4 correspond to $r = 0$, $r = d/2$, $r = 2d$ and $r = 3d$, respectively. The average flow velocities, (V_ϕ, V_r) , in mm/s were $(0,0)$, $(0.13, 0.19)$, $(3.81, 1.17)$, $(6.99, 0.89)$ for the curves 1 - 4, respectively.

FIG. 9. Snapshots of consecutive stages of mixing of a droplet of ink in the polymer solution in the half-size set-up, view from below. The area of the photographs corresponds to the area of the white upper plate. Rotation of the upper plate at $\Omega = 1.47 \text{ s}^{-1}$ ($\dot{\gamma} = 5.6 \text{ s}^{-1}$) was suddenly started at $t = 0$.

FIG. 10. Snapshots of consecutive stages of mixing of a droplet of ink in the pure solvent in the half-size set-up, view from below. Rotation of the upper plate at $\Omega = 1.47 \text{ s}^{-1}$ was suddenly started at $t = 0$.

FIG. 11. Average azimuthal velocity, \bar{V} , y -axis on the left, curves 1-3, and RMS of fluctuations of the azimuthal velocity, V_{rms} , y -axis on the right, curve 4, as functions of the distance, z , from the upper plate. The measurements were done at $r = 2d$. The average velocities are divided by the upper plate velocity at $r = 2d$. Curve 1 - polymer solution at $\dot{\gamma} = 2.7 \text{ s}^{-1}$; curves 2,4 polymer solution at $\dot{\gamma} = 4 \text{ s}^{-1}$ (see Fig.3-5, 8); curve 3 - pure solvent at $\dot{\gamma} = 4 \text{ s}^{-1}$, $Re \simeq 1.2$. The RMS of velocity fluctuations in the polymer solution, curve 4, is multiplied by λ/d to make it dimensionless.

FIG. 12. Probability distribution functions (PDF) of flow velocity measured at $r = 2d$, $z = d/4$ and $\dot{\gamma} = 4 \text{ s}^{-1}$, circles. Solid lines represent fits by Gaussians with some skewness. (a) azimuthal velocity, V_ϕ ; (b) radial velocity, V_r .

FIG. 13. Probability distribution functions (PDF) of velocity gradients measured at $r = 2d$, $z = d/4$ and $\dot{\gamma} = 4 \text{ s}^{-1}$, circles. The velocity gradients are made dimensionless by multiplication by the relaxation time, λ . Solid lines represent Gaussian fits. (a) longitudinal gradient, $\frac{\partial V_\phi}{r \partial \phi}$; (b) transversal gradient $\frac{\partial V_r}{r \partial \phi}$.

FIG. 14. Dependence of the upper plate stress ratio, τ_w/τ_w^{lam} , (actual polymer solution flow and a laminar flow with the same boundary conditions, cf. Fig.3) on the shear rate for a set-up with dimensions reduced four-fold compared with the standard configuration of the flow between two plates. Black and gray curves correspond to raising and decreasing shear rate respectively.

FIG. 15. Mixing patterns in polymer solution flow in set-ups with flow between two plates and with dimensions reduced two-fold (left column) and four-fold (right column) compared with the standard configuration. Photographs in consecutive rows were taken at equal times elapsed from sudden inception of the upper plate rotation at $\Omega = 1.47 \text{ s}^{-1}$ ($\dot{\gamma} = 5.6 \text{ s}^{-1}$). Images in the right column are magnified by a factor of two to match the sizes. The area of the photographs corresponds to the area of the white upper plate.

FIG. 16. Power, P , of velocity fluctuations in set-ups with flow between two plates as function of frequency, f . Curves 1 and 3 are for the radial velocity component, V_r , and curves 2 and 4 are for the azimuthal velocity, V_ϕ . Black curves (1 and 2) are for the standard set-up, and gray curves (3 and 4) are for a set-up with two-fold reduced dimensions.

FIG. 17. Schematic drawing on the Couette-Taylor set-up, mounted on top of the AR-1000 rheometer. A circular cap with a hole for the rotating shaft, which covered the glass cylinder from above, is not shown.

FIG. 18. The ratio of average shear stress in the actual flow of the polymer solution and the stress corresponding to a laminar flow with the same $\dot{\gamma}$, τ/τ_{lam} , as a function of the Weissenberg number, $Wi = \lambda R_1 \Omega / d$. Thin black line: increasing rotation rate, starting from $Wi = 0.7$; thick gray line: decreasing rotation rate, starting from $Wi = 7$.

FIG. 19. Power of fluctuations of the radial component of the flow velocity, V_r , measured at $r = (R_1 + R_2)/2$, as a function of frequency, f . Curves 1-4 correspond to $Wi = 8.5, 13.6, 21.8$ and 35 , respectively. Two power law fits for curve 4 in different regions are shown to guide the eye.

FIG. 20. Probability distribution functions of the radial component of the flow velocity, V_r , measured at $r = (R_1 + R_2)/2$, at different Wi . Curves 1-4 correspond to $Wi = 5.4, 13.6, 21.8$ and 35 , respectively.

FIG. 21. Schematic drawing of the curvilinear channel showing the inlet, a region of observation, and the outlet.

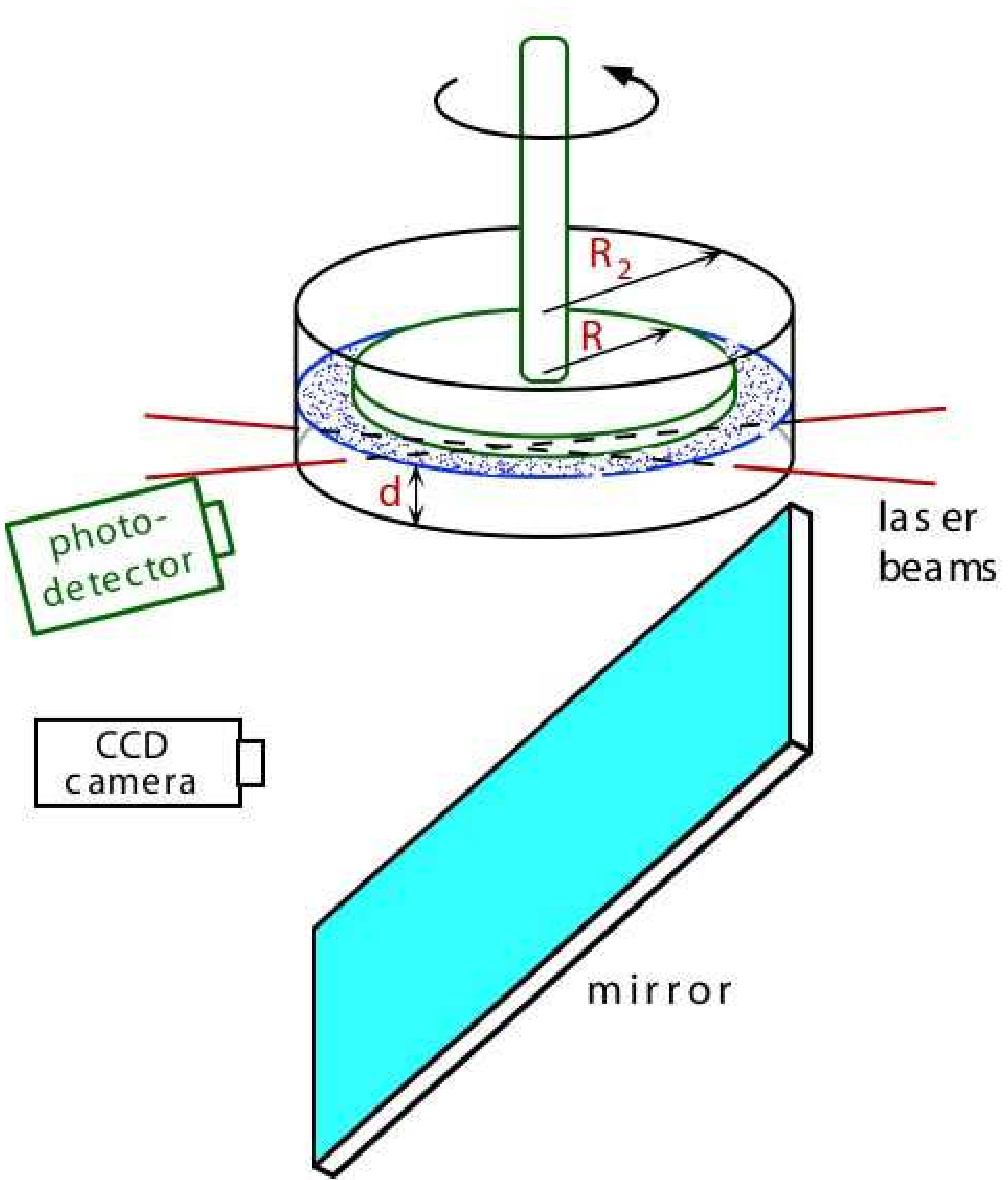
FIG. 22. Photographs of the flow taken with the laser sheet visualization (Fig.21) at different N . The field of view is 3.07 by 2.06 mm, and corresponds to the region shown in Fig.21 (rotated 90° counterclockwise). Bright regions correspond to high concentration of the fluorescent dye. (a) flow of the pure solvent at $N = 29$; (b, c, d) flow of the polymer solution at $Wi = 6.7$ and at $N = 8, 29, 54$, respectively.

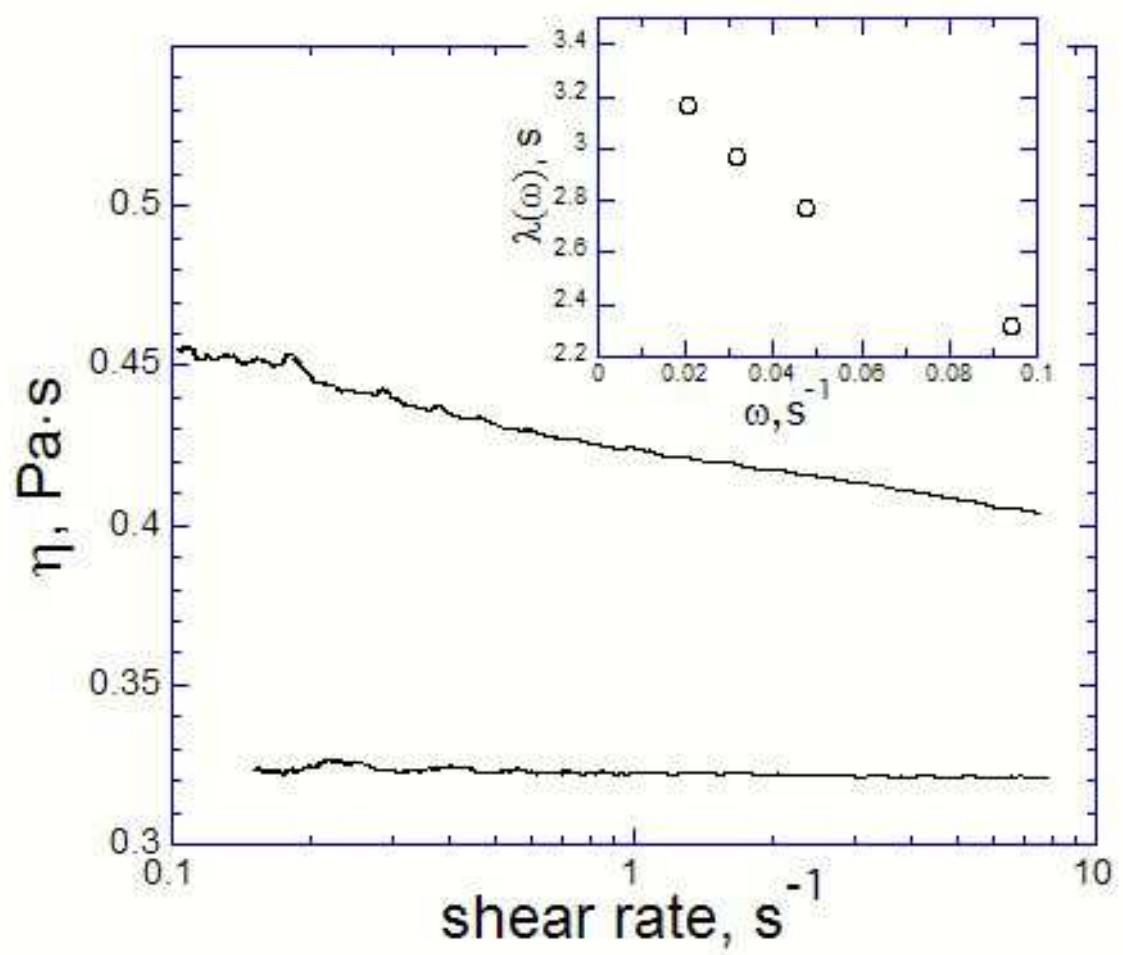
FIG. 23. Representative space-time diagrams of the polymer solution flow at $Wi = 6.7$ taken at different positions, N , along the channel.

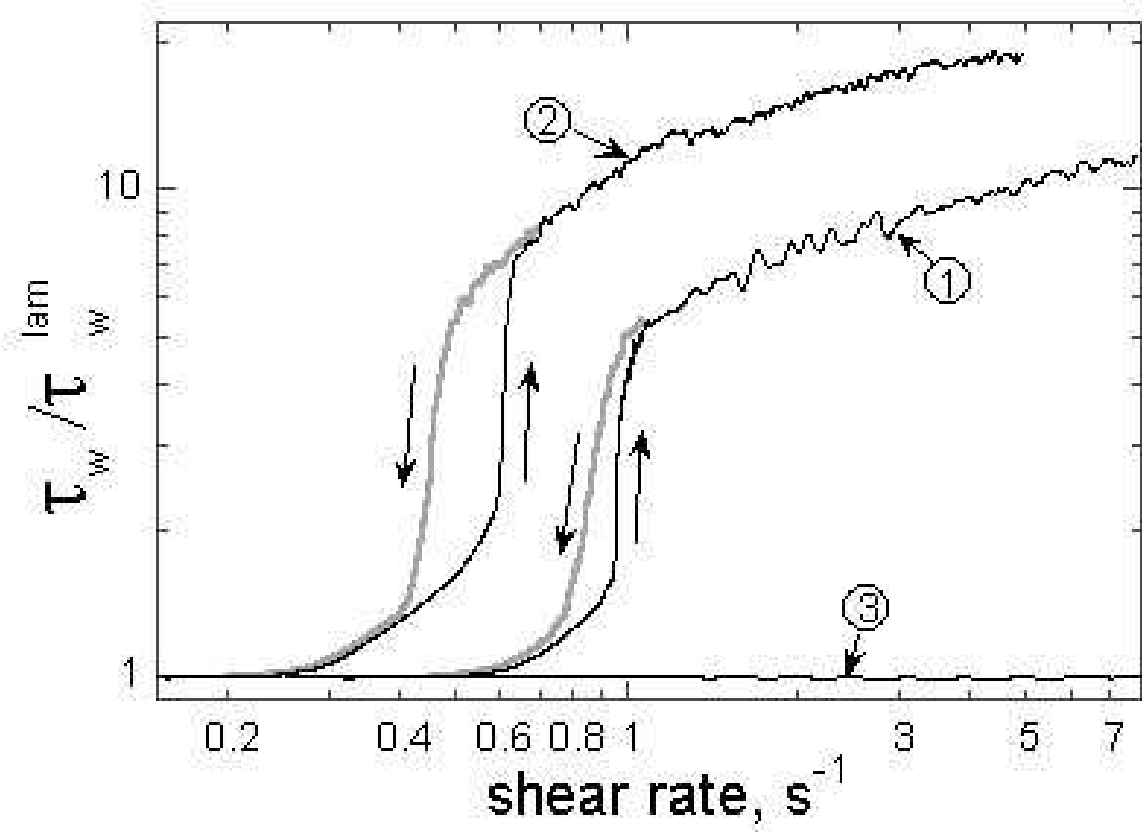
FIG. 24. Dependence of c_{rms} (normalized root mean square of concentration deviations from the average) on the Weissenberg number, Wi , measured near the channel exit at $N = 29$ (semi-logarithmic coordinates).

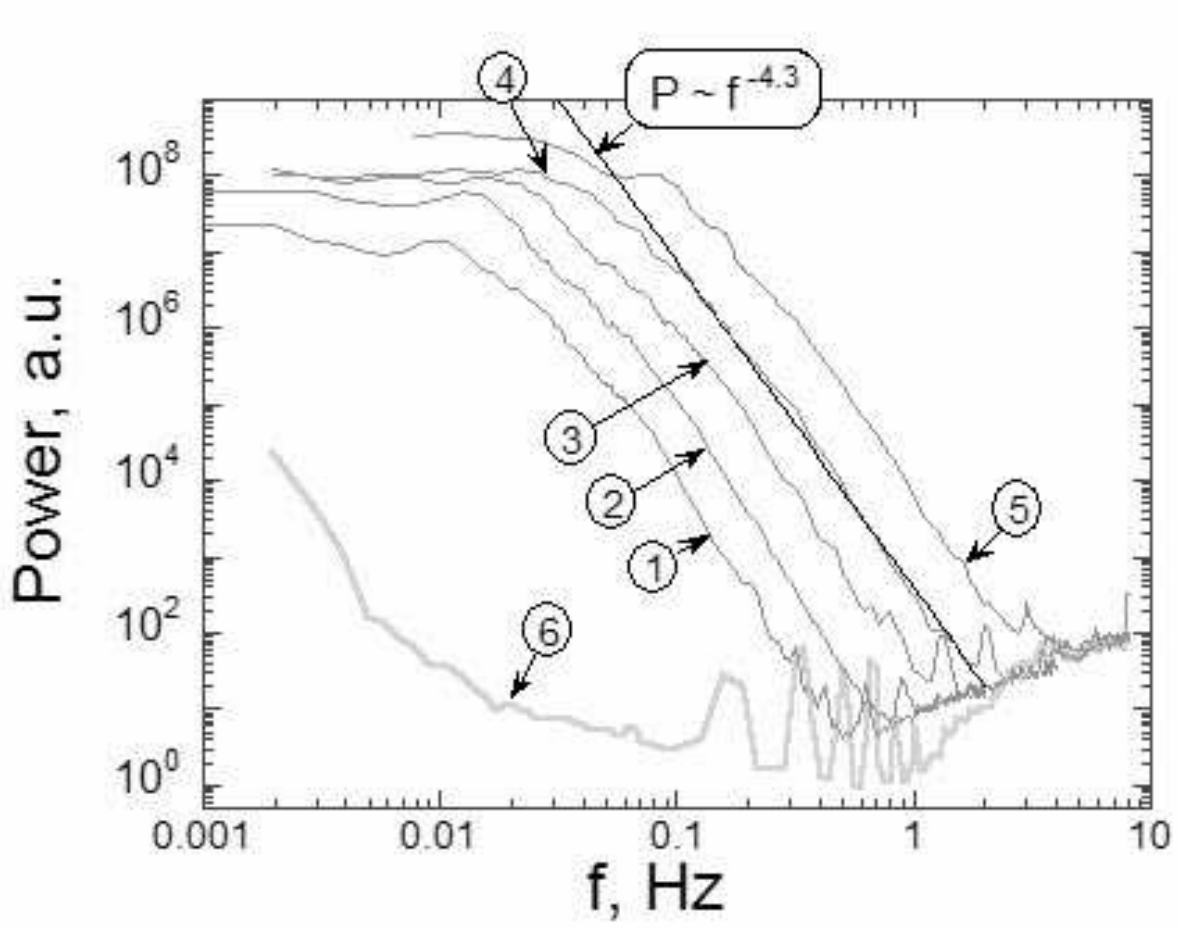
FIG. 25. Power, P , of fluctuations of velocity in the middle of the channel at $N = 12$ as a function of frequency, f . The spectra in the polymer solution flow at $Wi = 6.7$ for the velocity components along and across the mean flow are shown by curves 1 and 2, respectively. Curve 3 shows velocity spectrum across the mean flow for the pure solvent at the same Q .

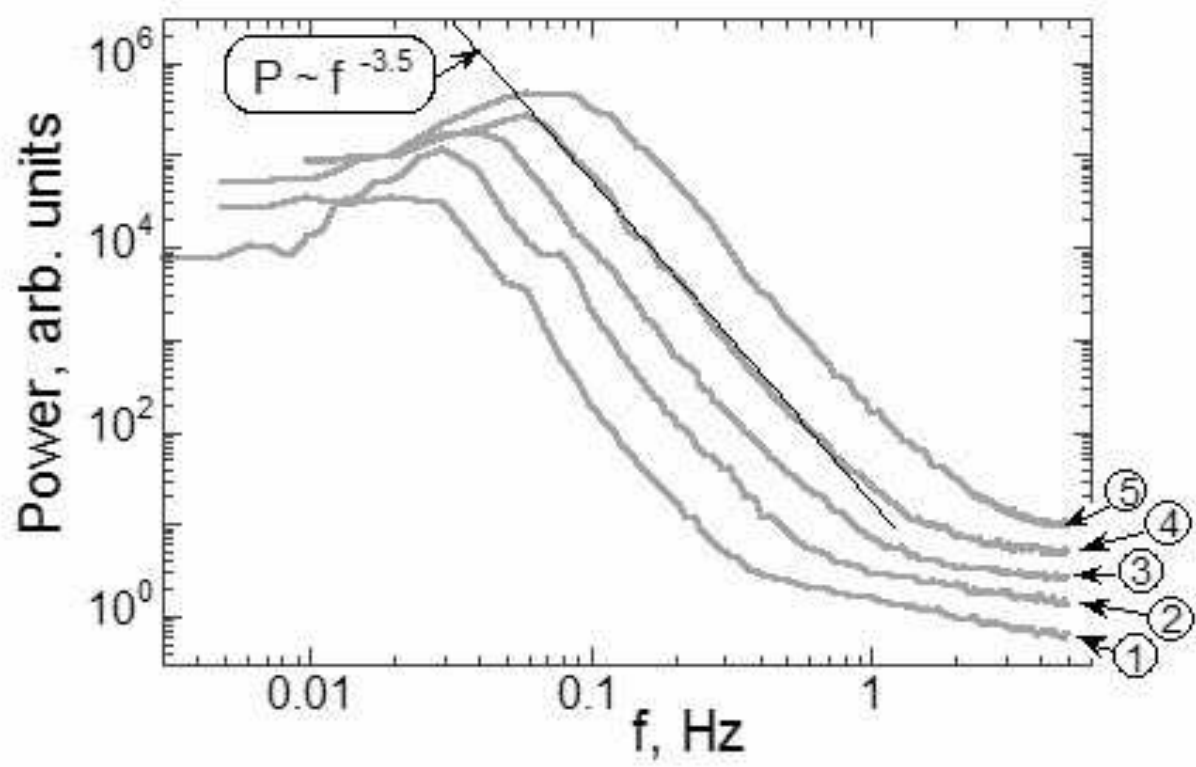
FIG. 26. Ratio of a pressure drop across the channel in the polymer solution flow, ΔP , to a pressure drop for a laminar flow, ΔP_{lam} , as a function of rate of liquid discharge, Q (in semi-logarithmic coordinates).

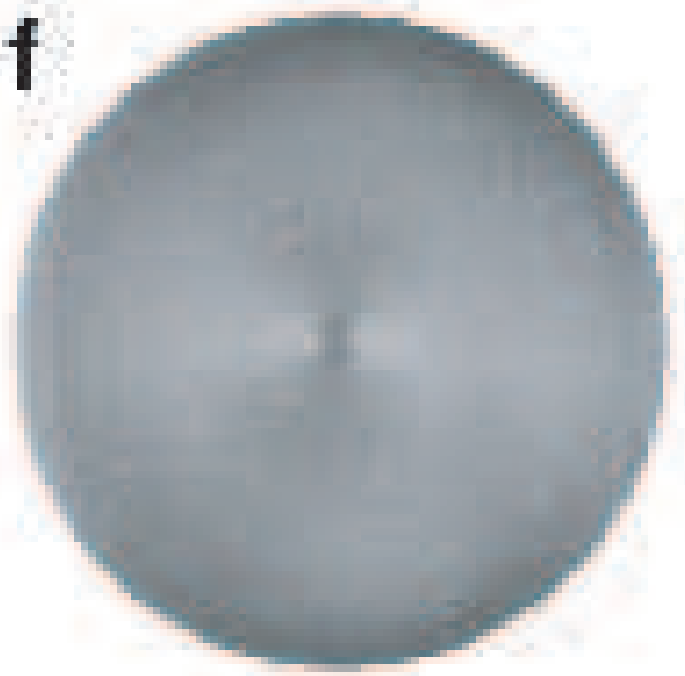
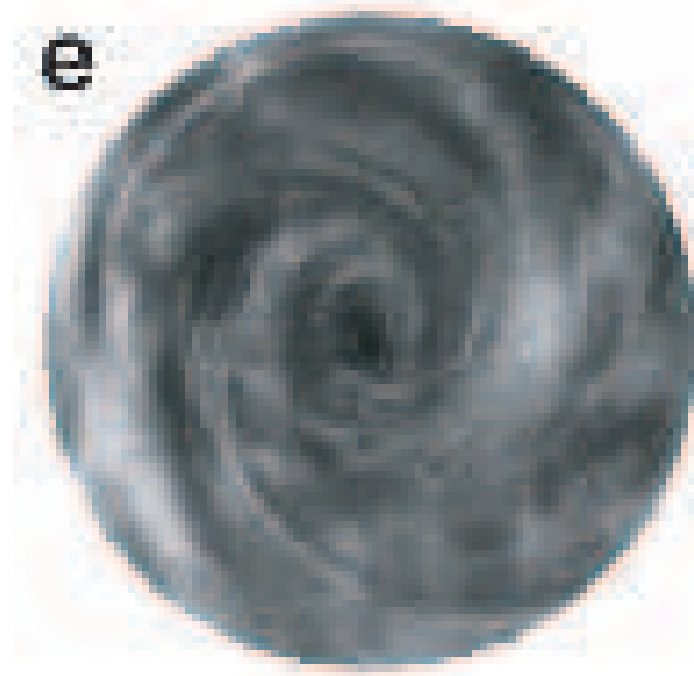
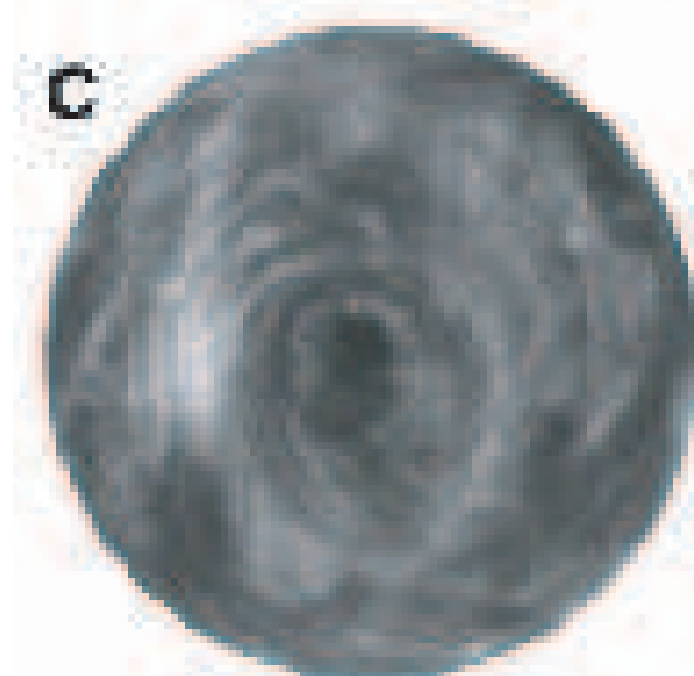
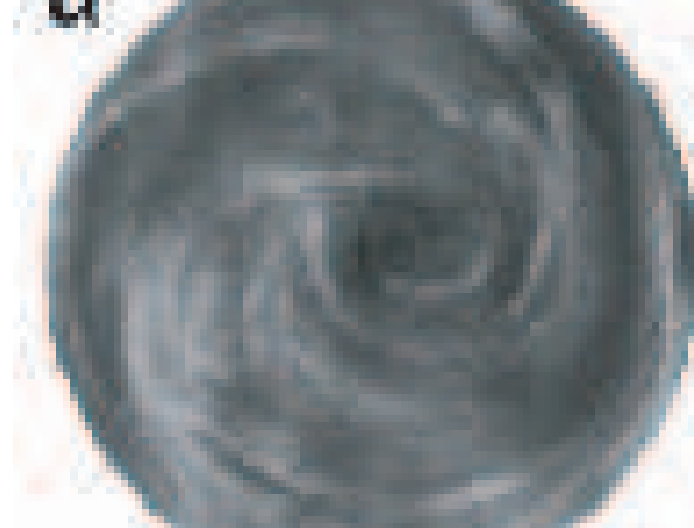


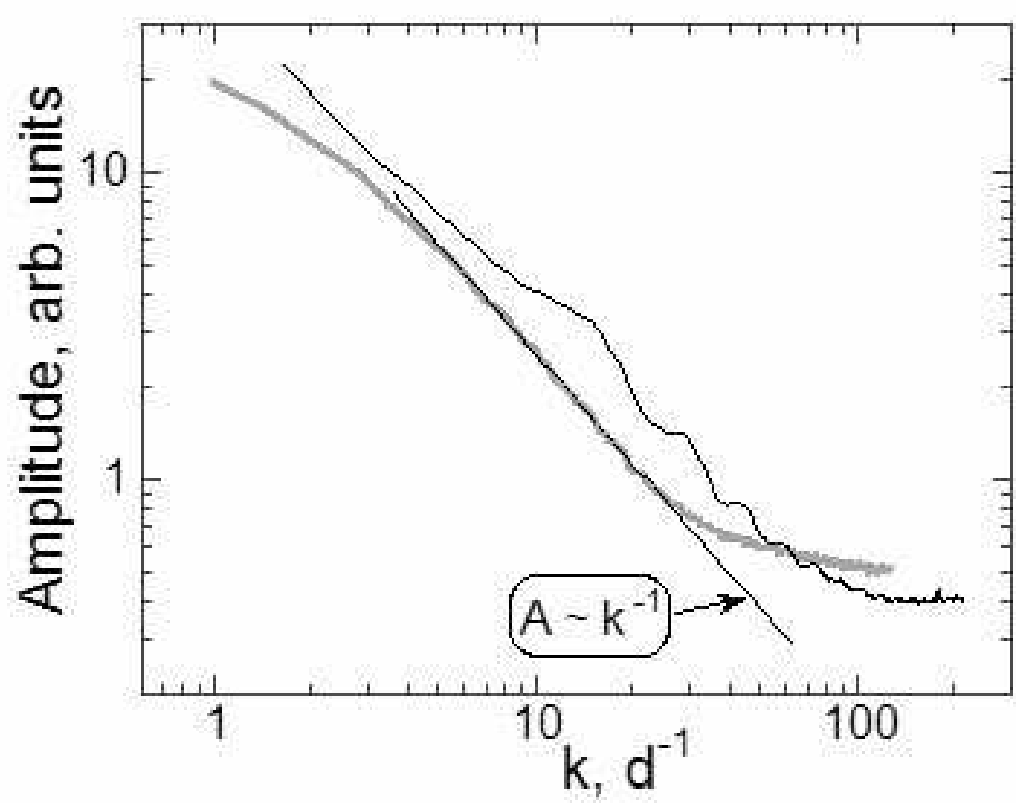


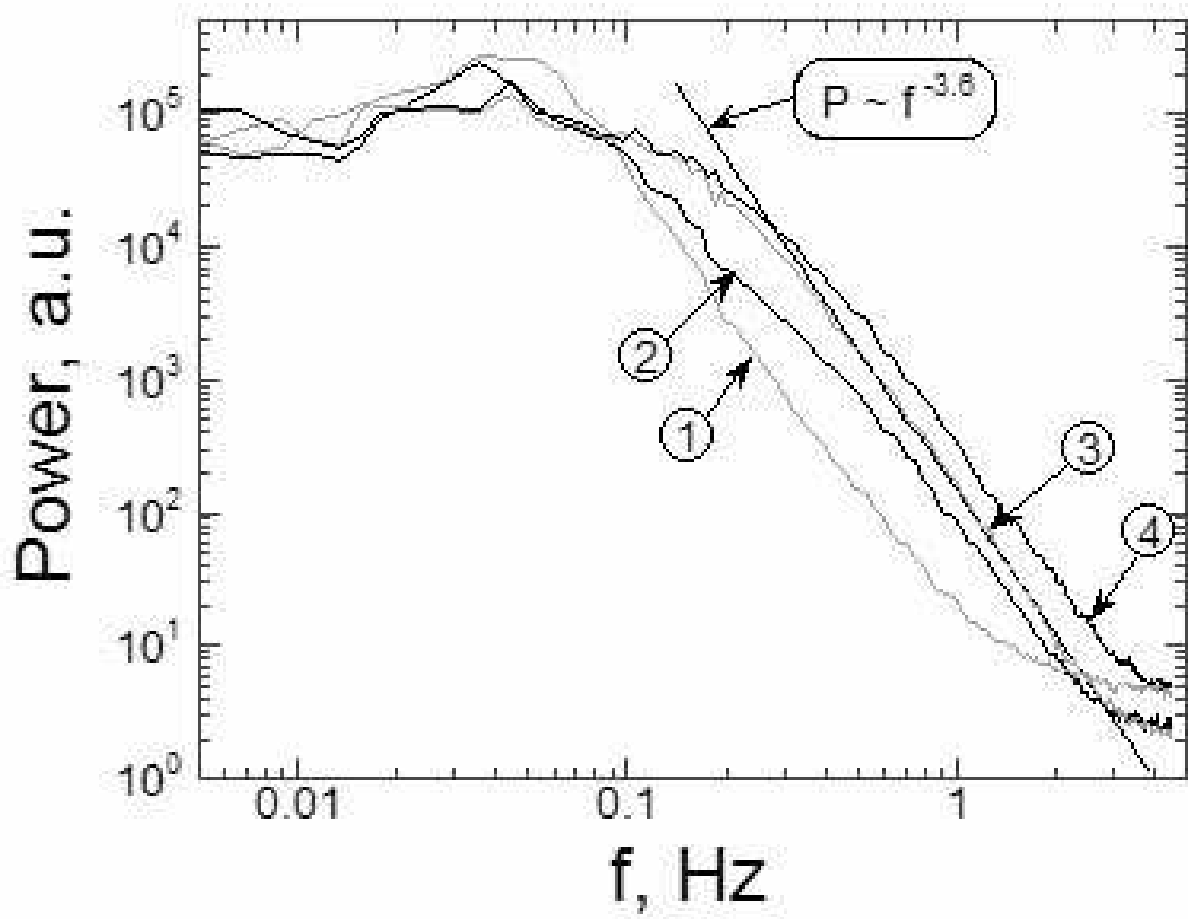










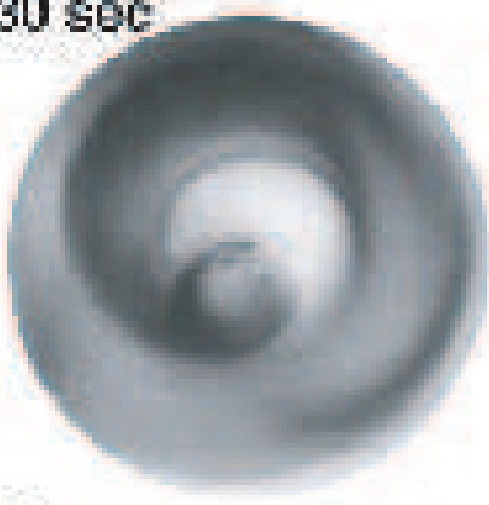




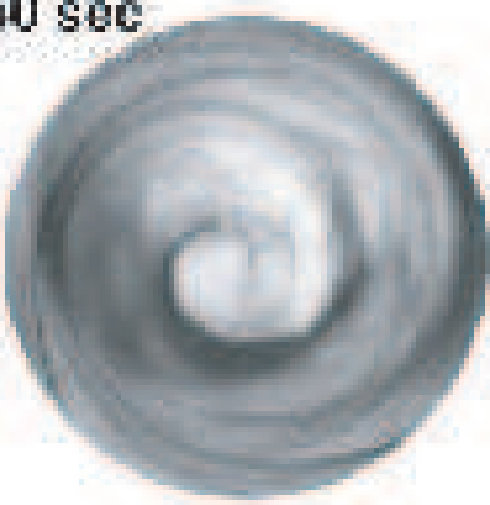
30 sec



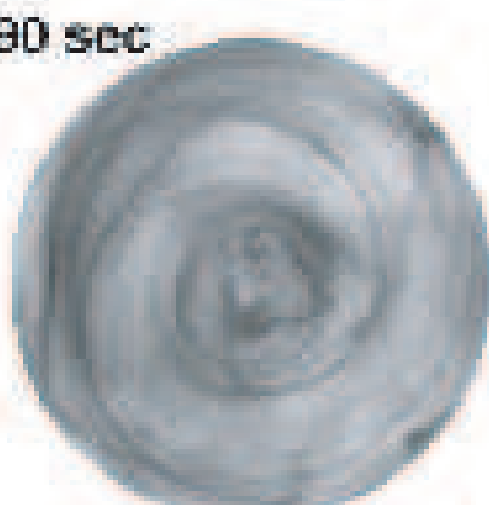
60 sec



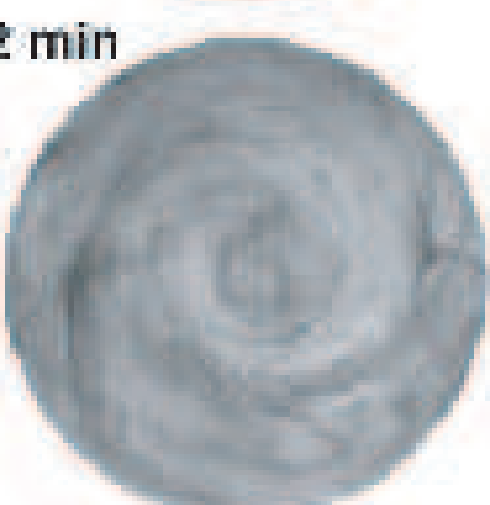
90 sec



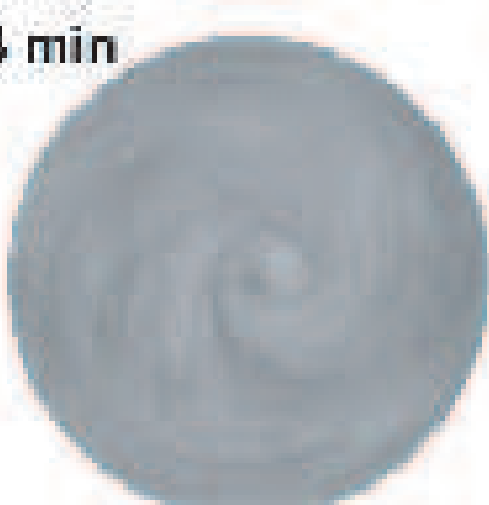
2 min



4 min



8 min



t=0

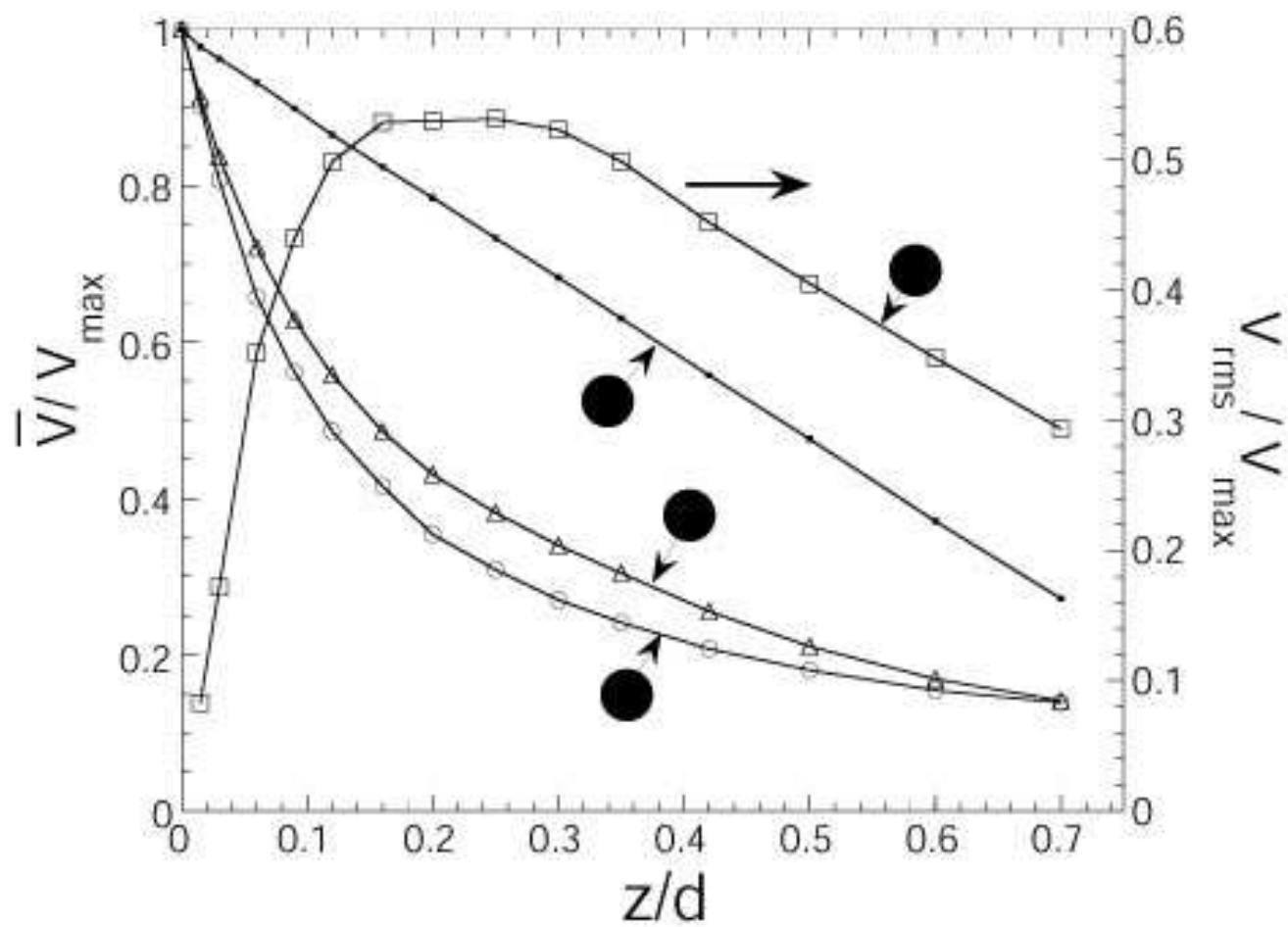
4 min

15 min

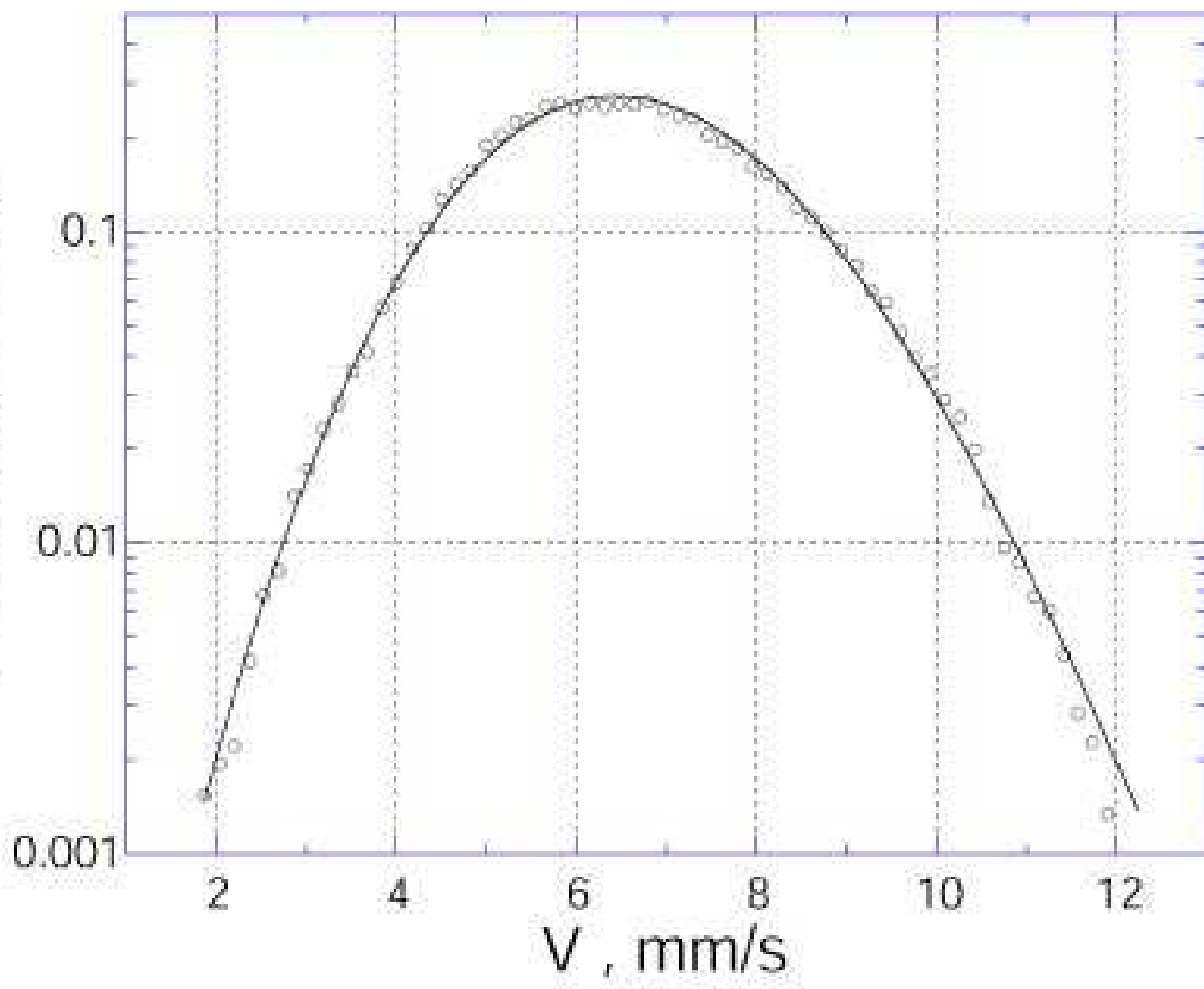
1 hr

2 hr

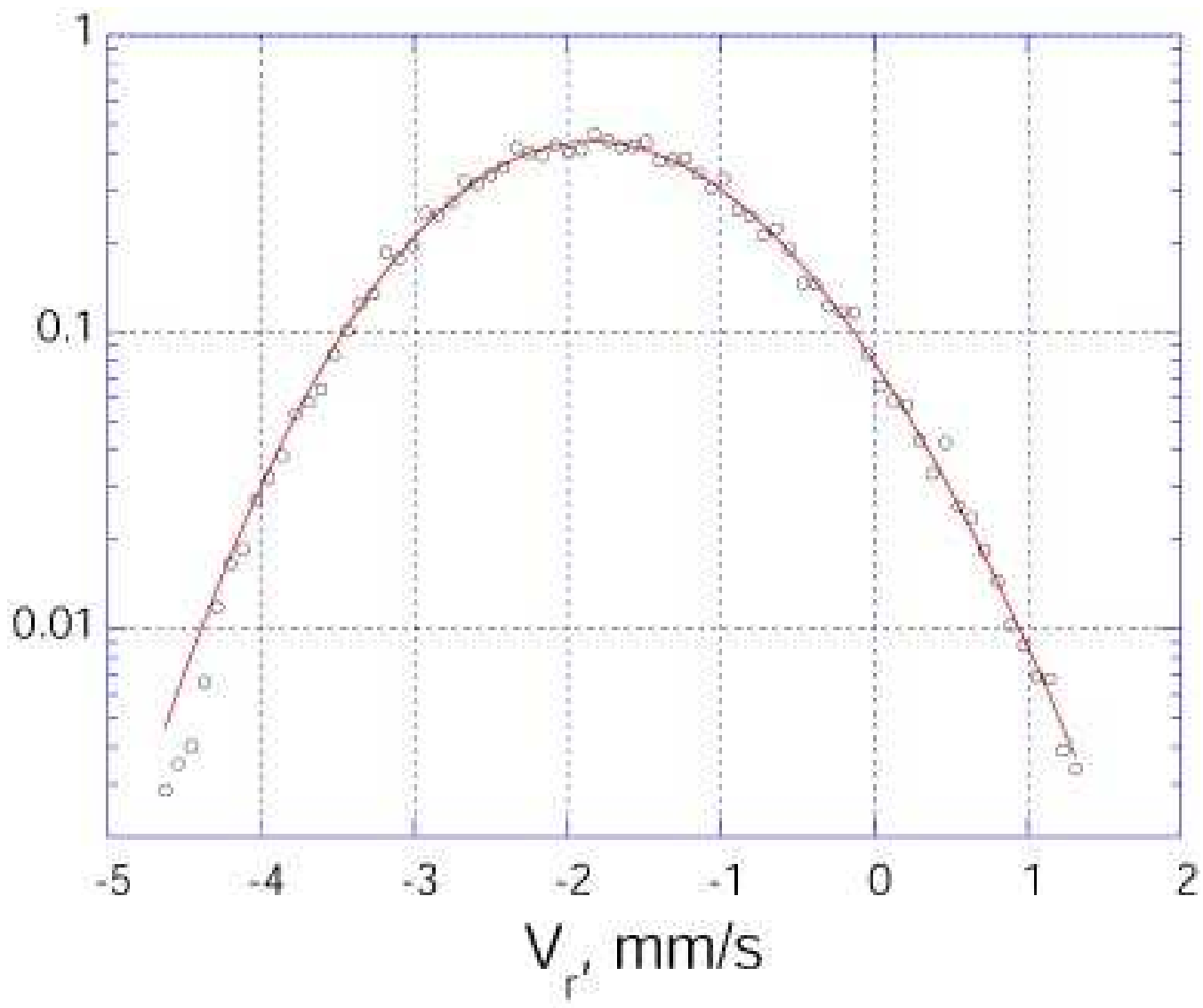
9 hr



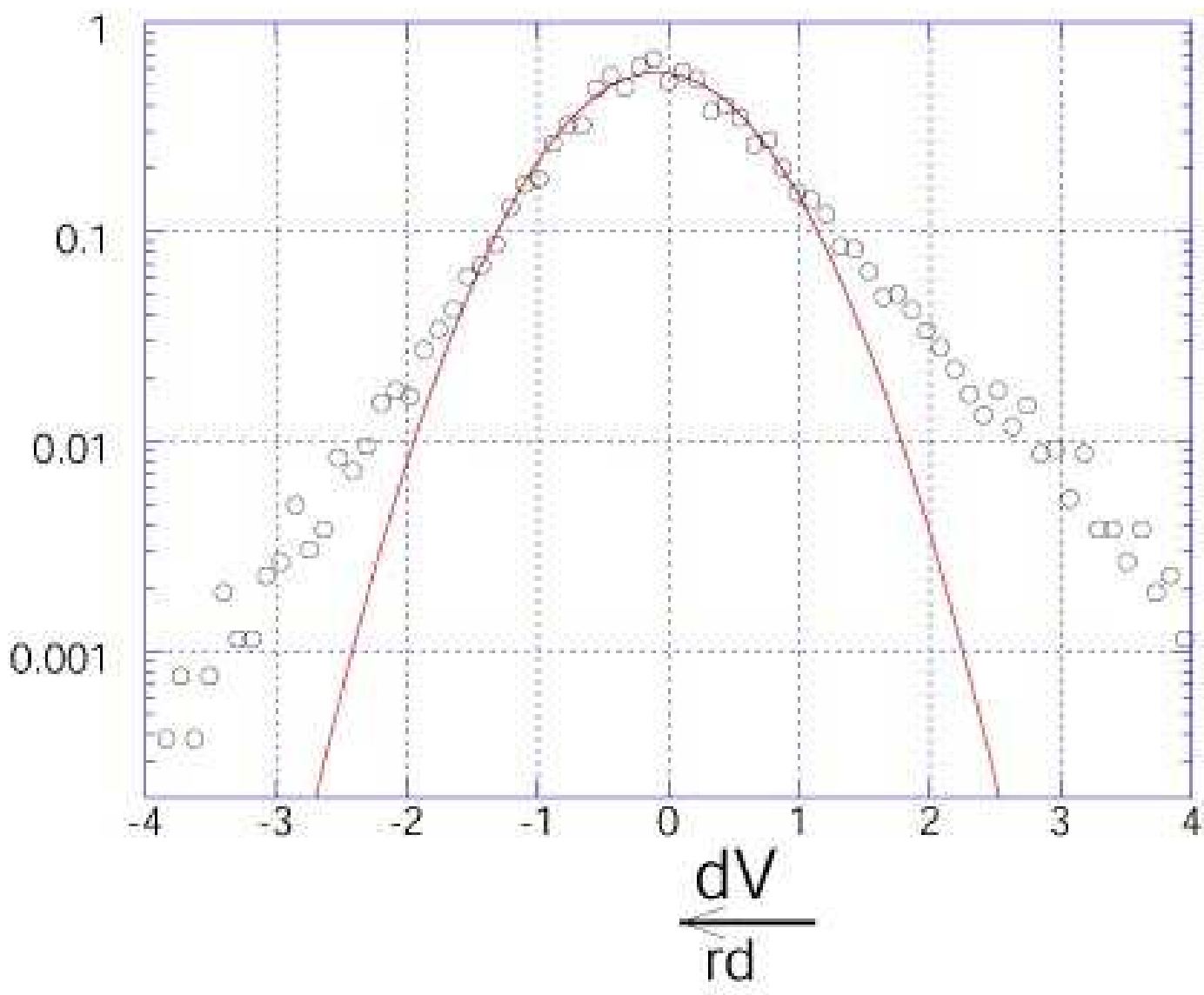
Probability density



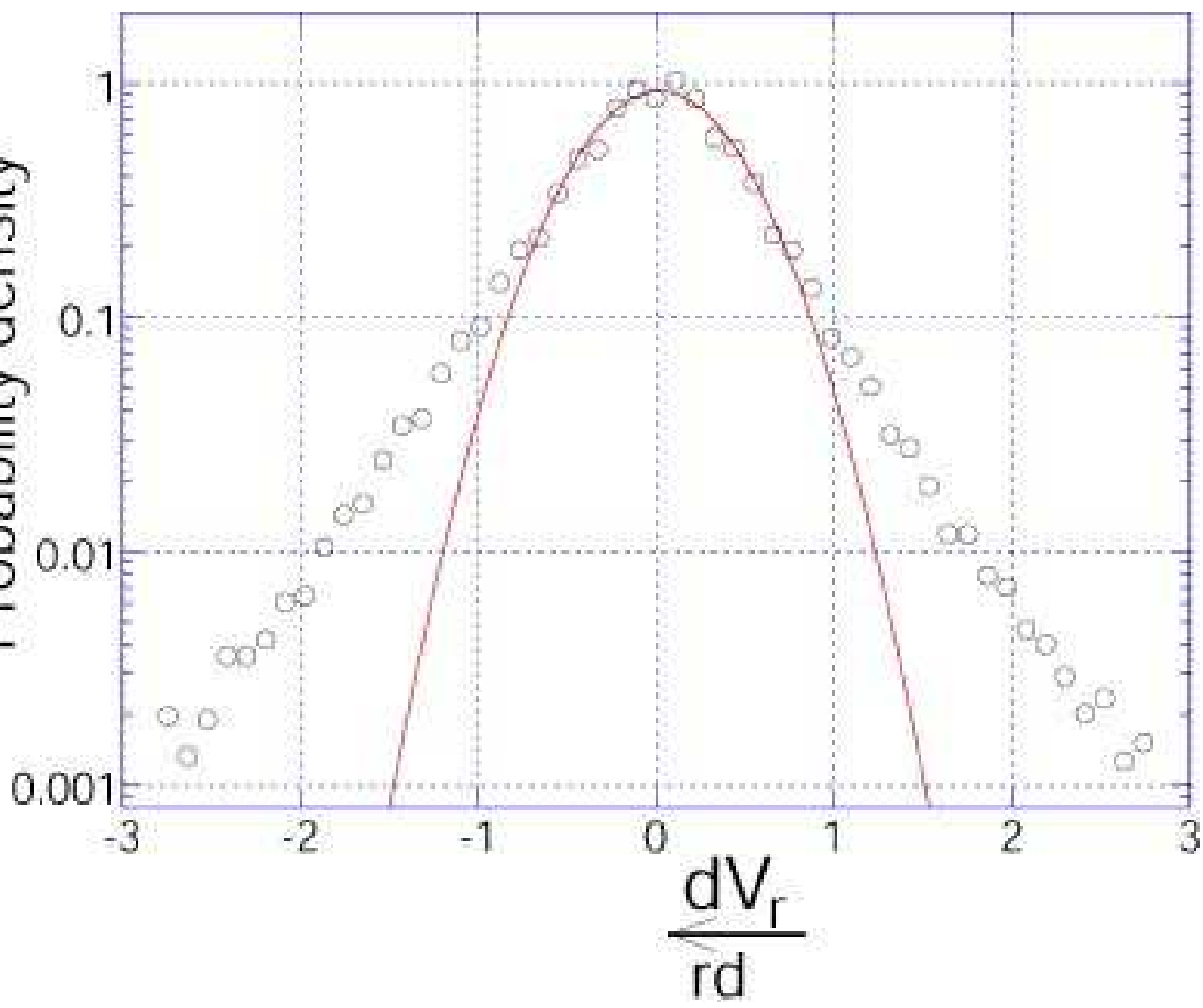
Probability density

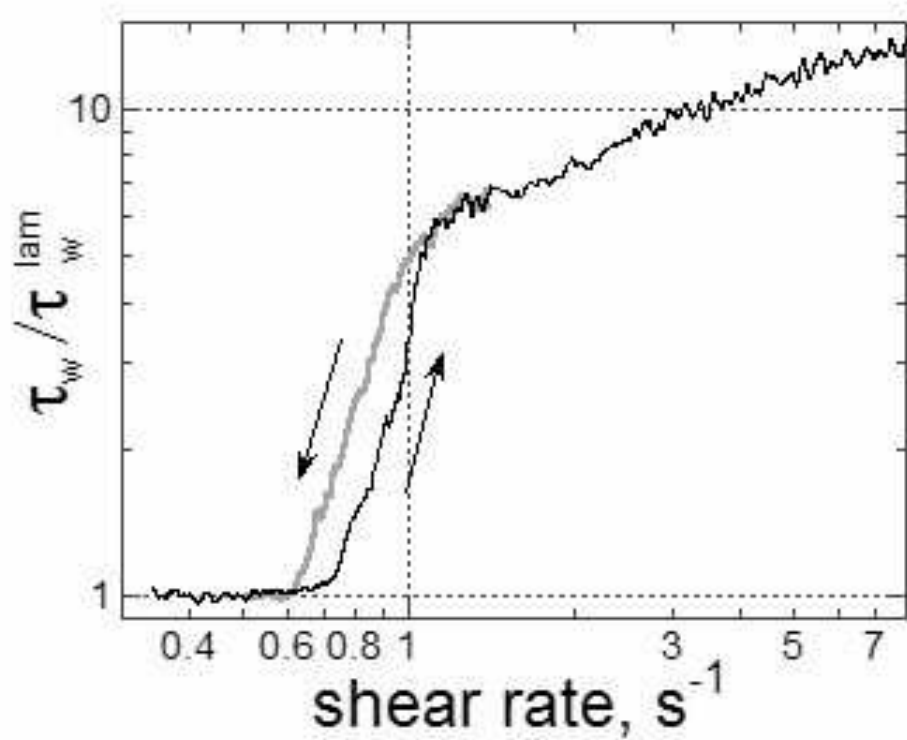


Probability density



Probability density







60 sec

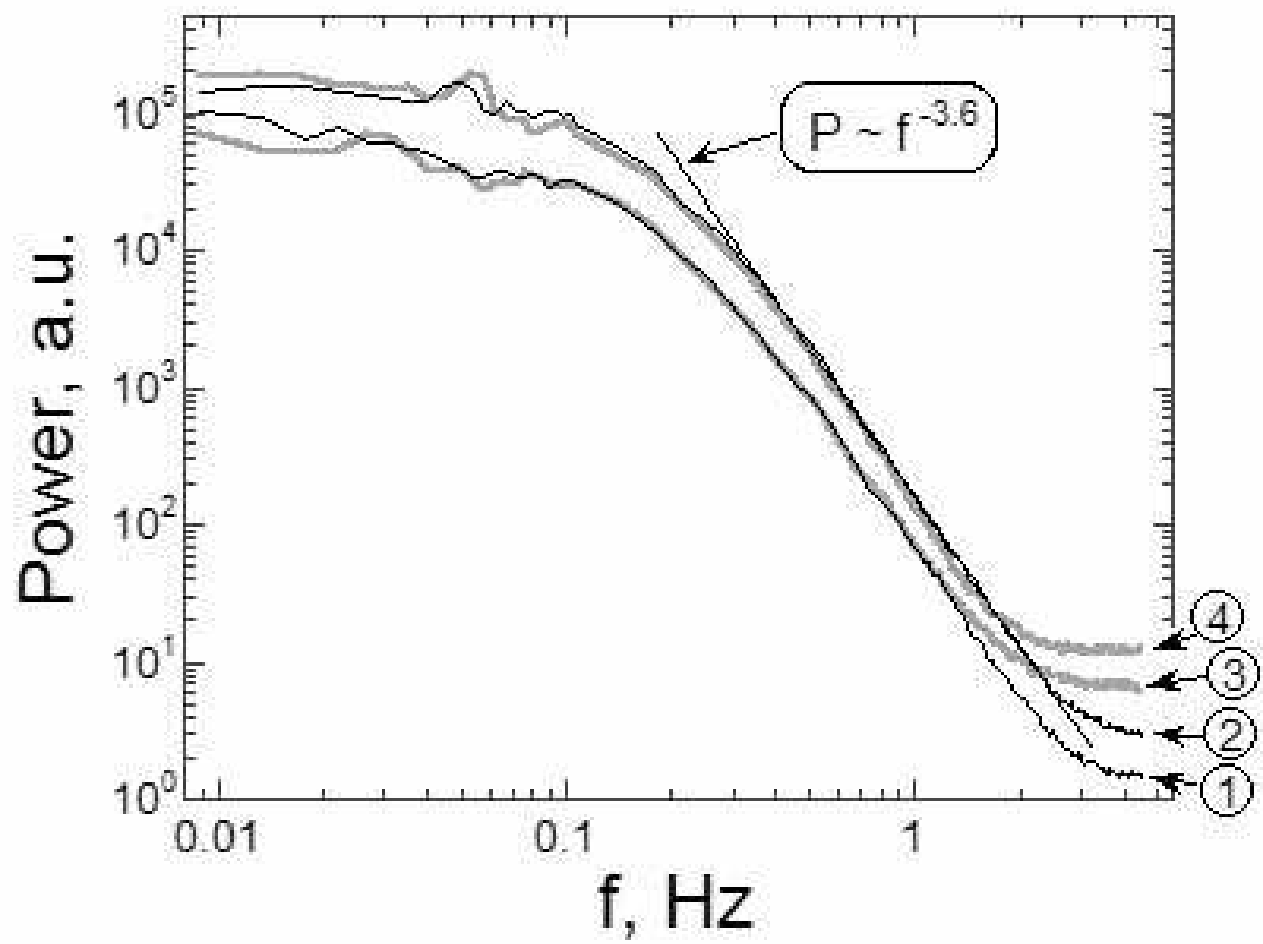


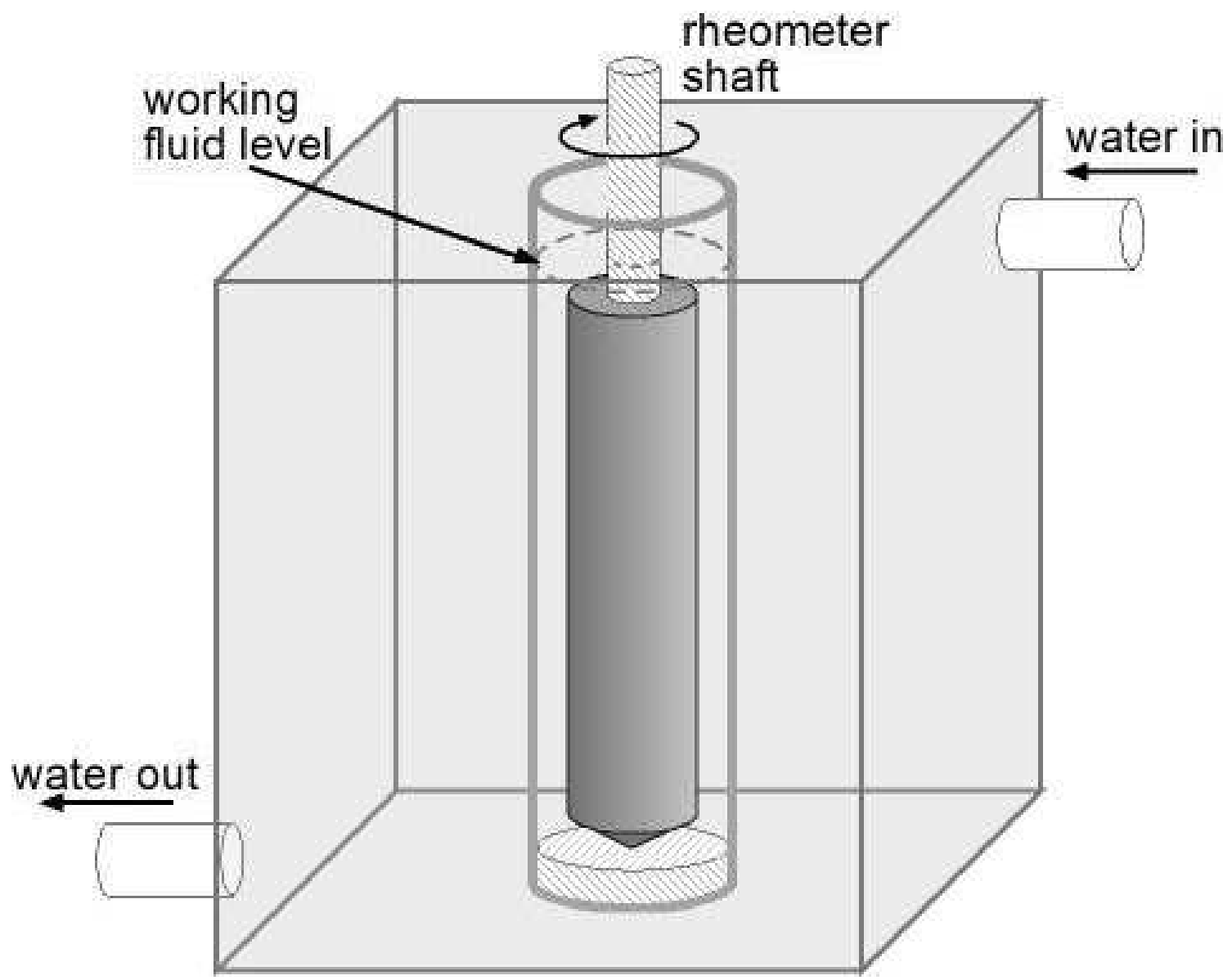
90 sec

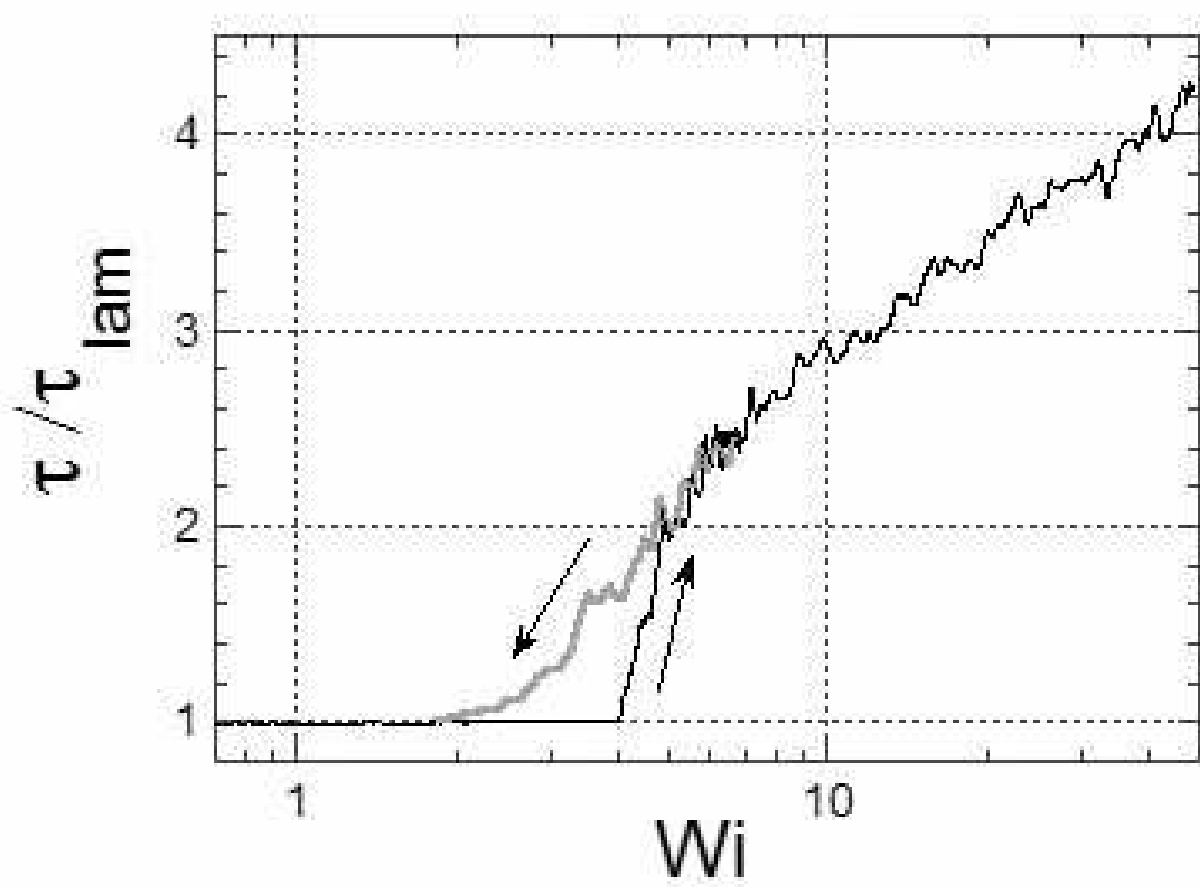


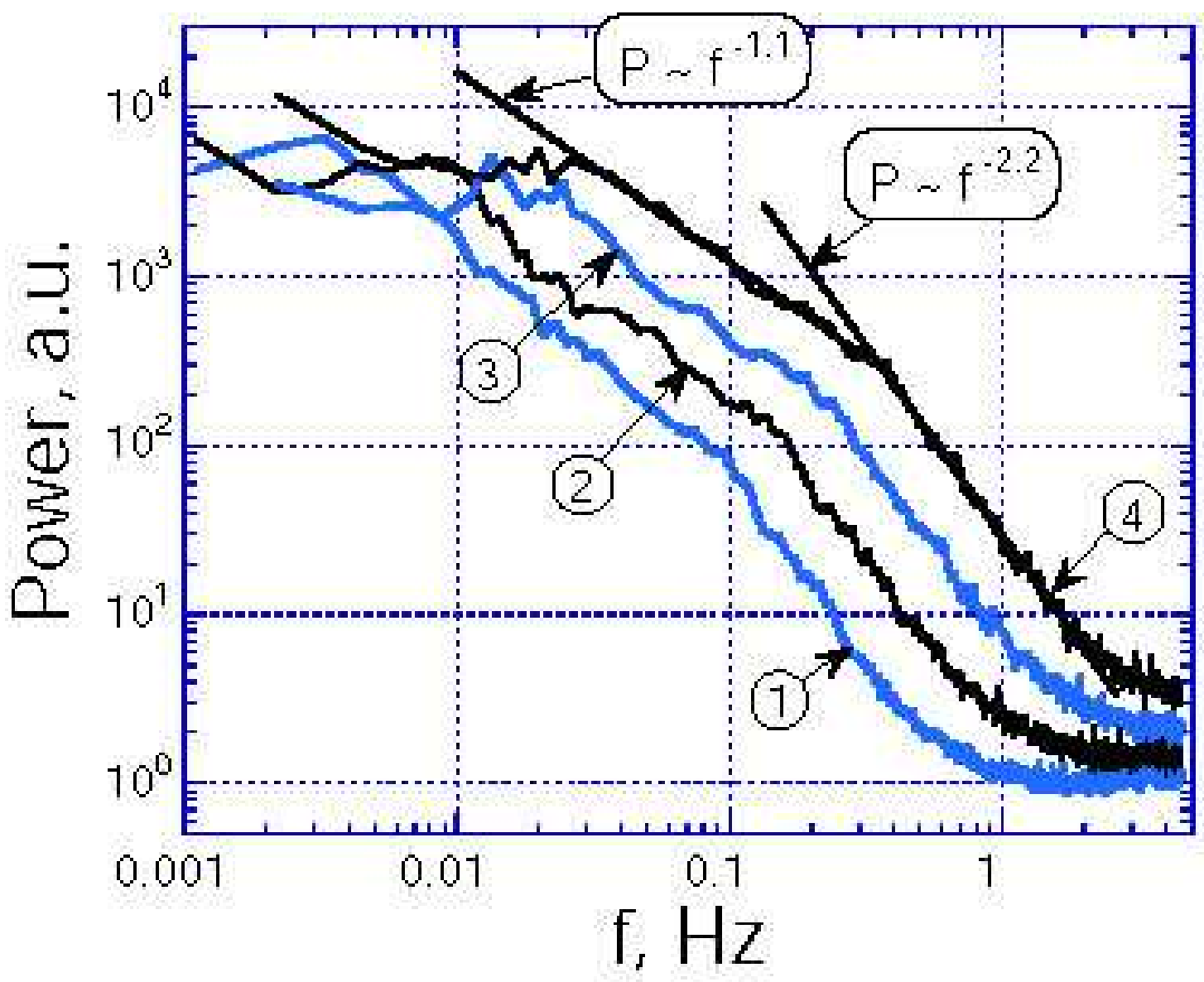
120 sec

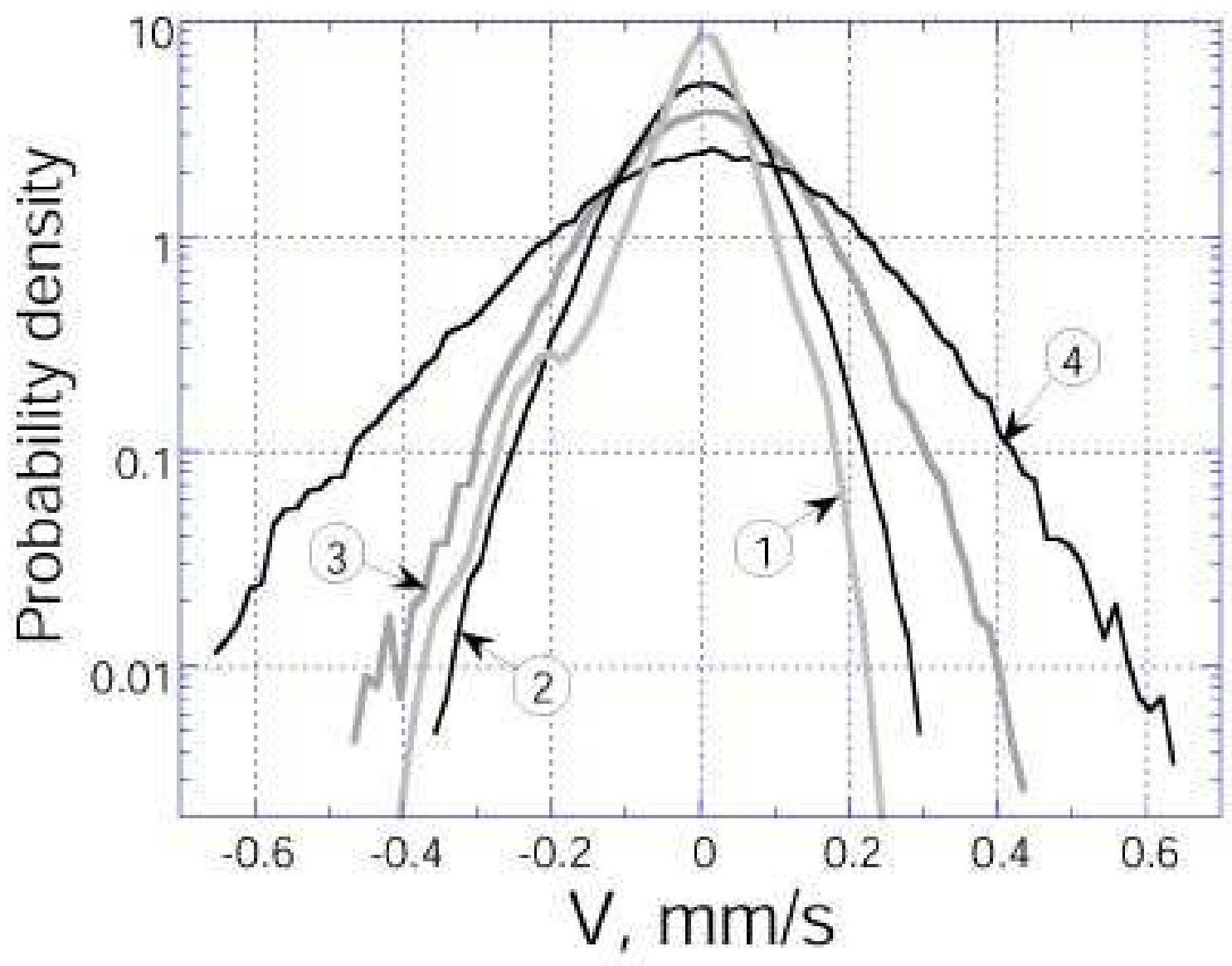


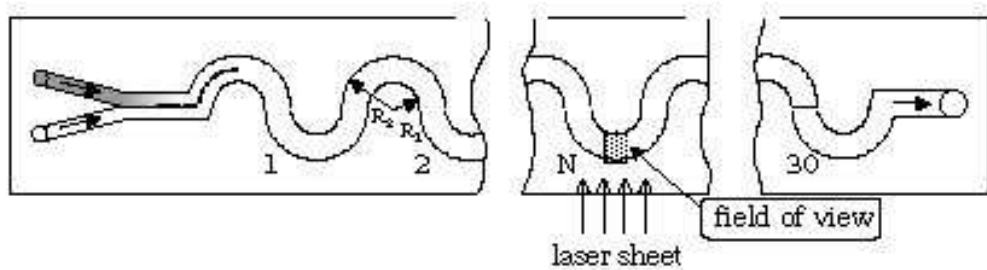


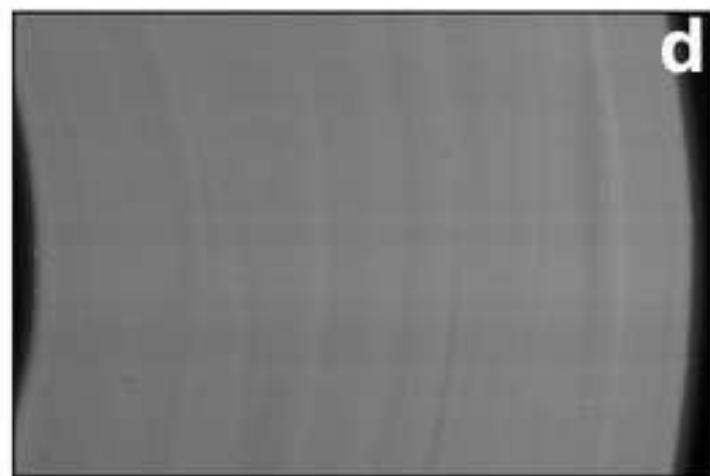
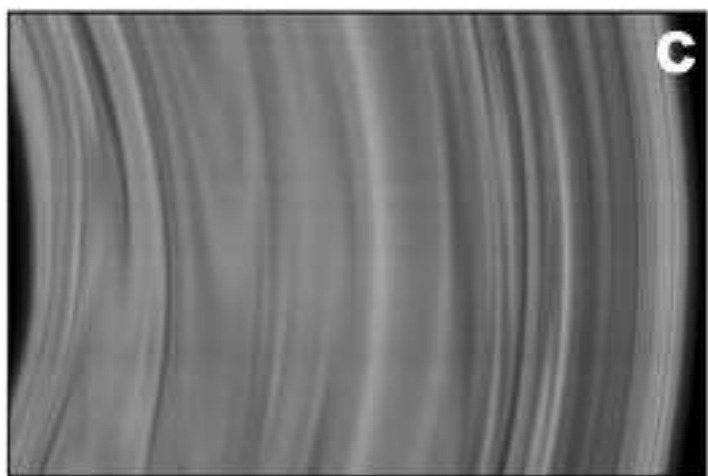
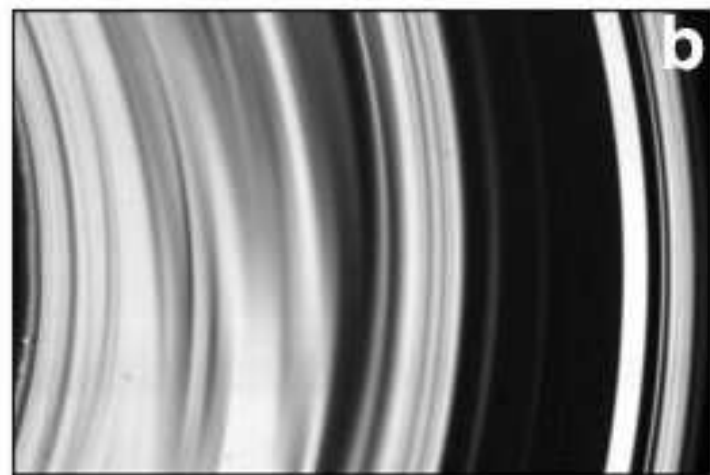




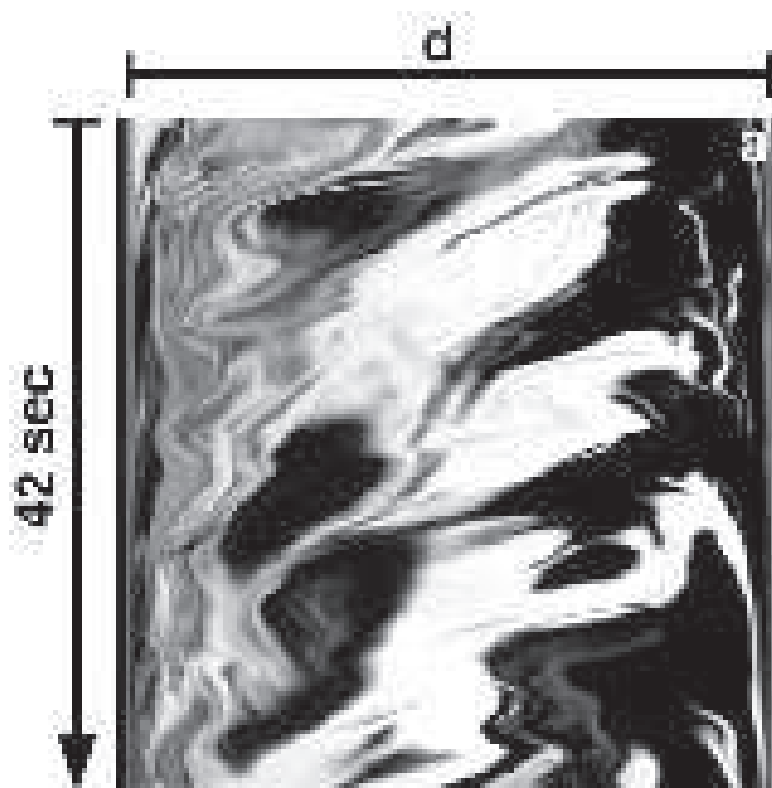






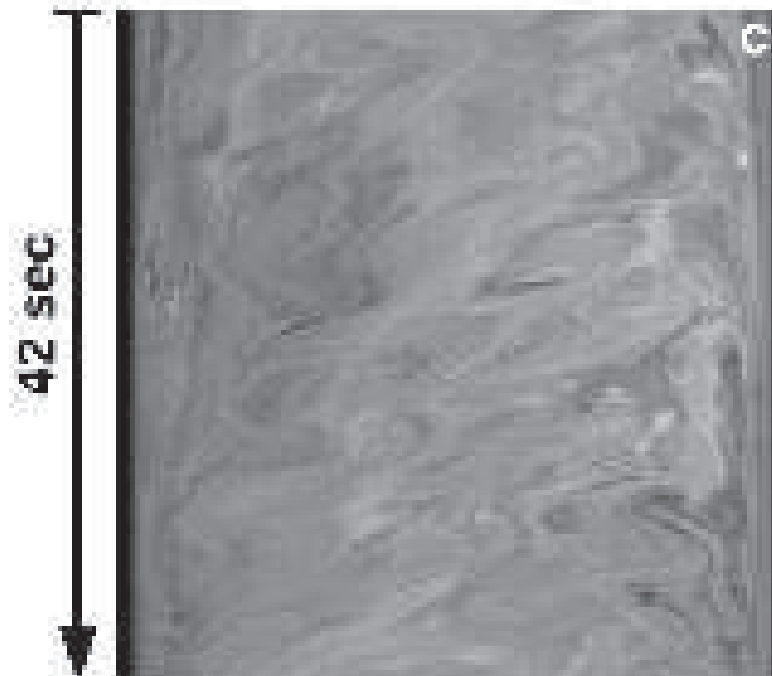


42 sec

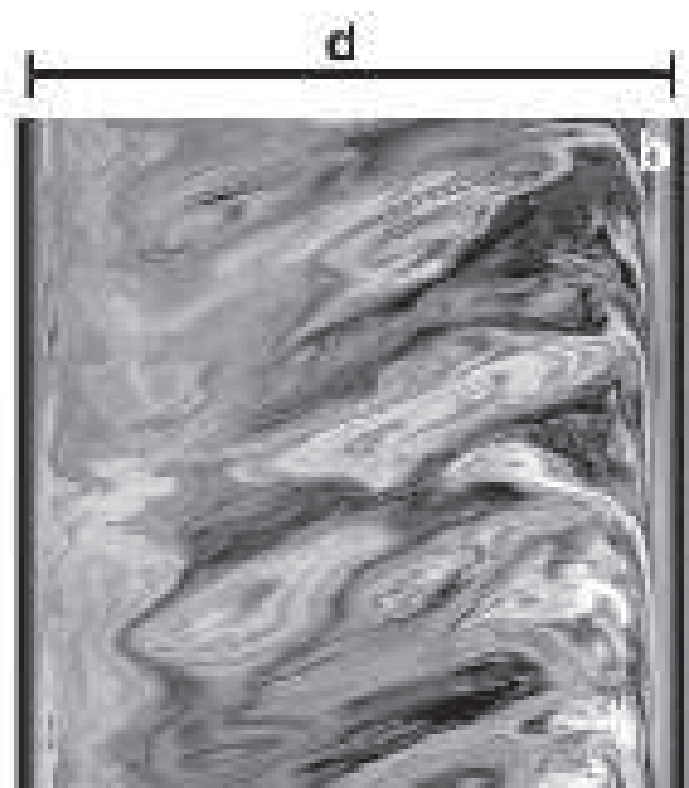


N=6

42 sec



N=39



N=24



N=54

